

Article

Seeps and Tectonic Structure of the Hydrothermal System of the Panarea Volcanic Complex (Aeolian Islands, Tyrrhenian Sea)

Federico Spagnoli ^{1,2,3,*} , Teresa Romeo ^{4,5} , Franco Andaloro ⁶, Simonepietro Canese ⁶, Valentina Esposito ⁷ , Marco Grassi ⁸, Erik Delos Biscotti ⁸, Patrizia Giordano ⁹  and Giovanni Bortoluzzi ^{3,†}

¹ IRBIM-CNR, Istituto per le Risorse Biologiche e le Biotecnologie Marine—Consiglio Nazionale delle Ricerche, 60125 Ancona, Italy

² Sezione di Geologia, Scuola di Scienze e Tecnologia, Università di Camerino, 62032 Camerino, Italy

³ ISMAR-CNR, Istituto di Scienze Marine—Consiglio Nazionale delle Ricerche, 40129 Bologna, Italy; giovanni.bortoluzzi@cnr.it

⁴ Department of Biology and Evolution of Marine Organisms, Stazione Zoologica Anton Dohrn, Sicily, Marine Centre, 98167 Messina, Italy; teresa.romeo@szn.it

⁵ National Institute for Environmental Protection and Research, 98057 Milazzo, Italy

⁶ Stazione Zoologica Anton Dohrn, 80121 Napoli, Italy; franco.andaloro@szn.it (F.A.); simone.canese@szn.it (S.C.)

⁷ Istituto Nazionale di Oceanografia e di Geofisica Sperimentale—OGS, 34010 Trieste, Italy; vesposito@ogs.it

⁸ Marina Militare—Istituto Idrografico della Marina, 16163 Genova, Italy; marco.grassi@marina.difesa.it (M.G.); erikd.biscotti@marina.difesa.it (E.D.B.)

⁹ ISP, Istituto di Scienze Polari—Consiglio Nazionale delle Ricerche, 40129 Bologna, Italy; patrizia.giordano@cnr.it

* Correspondence: federico.spagnoli@cnr.it

† Deceased.

Abstract: High-definition bathymetry mapping, combined with the measurement of dissolved benthic fluxes and water column biogeochemical properties, allows for a description of new biogeochemical processes around the Panarea Volcanic island. Investigations focused on the CO₂ releases from the bottom sea on the east of the Panarea volcanic complex provided insights into the geological setup of the marine area east and south of the Panarea Island. Between the Panarea Island and the Basiluzzo Islet lies a SW-NE-stretching graben structure where a central depression, the Smoking Land Valley, is bounded by extensional faults. Abundant acidic fluids rich in dissolved inorganic Carbon are released on the edges of the graben, along the extensional faults, either diffusely from the seafloor, from hydrothermal chimneys, or at the center of craters of different sizes. The precipitation of iron dissolved in the acidic fluids forms Fe-oxyhydroxides bottom sea crusts that act as a plug, thus preventing the release of the underlying gases until their mounting pressure generates a bursting release. This process is cyclic and results in intermittent gas release from the bottom, leaving extinct craters and quiescent chimneys. The measurement of dissolved benthic fluxes allowed us to estimate the volcanic DIC venting at 15 Mt of CO₂ over the past 10,000 years. The fluxes are not distributed homogeneously but rather concentrate along fractures and fault planes, which facilitate their rise to the seafloor. The acidic fluids released affect the chemical properties and structure of the water column through the formation of layers with a lower pH under the pycnocline, which can limit volcanic CO₂ release to the atmosphere. Further and continuous monitoring and investigation of the area are needed in order to complete a thorough picture of the variations in fluid releases through time and space. The importance of such monitoring lies in the development of a new method for detecting and quantifying the diffusive dissolved benthic fluxes on a volcanic sea bottom affected by hydrothermal seeps.

Keywords: benthic fluxes; hydrothermal system; CO₂; Panarea volcanic complex; marine biogeochemistry



Citation: Spagnoli, F.; Romeo, T.; Andaloro, F.; Canese, S.; Esposito, V.; Grassi, M.; Biscotti, E.D.; Giordano, P.; Bortoluzzi, G. Seeps and Tectonic Structure of the Hydrothermal System of the Panarea Volcanic Complex (Aeolian Islands, Tyrrhenian Sea). *Geosciences* **2024**, *14*, 60. <https://doi.org/10.3390/geosciences14030060>

Academic Editors: Jesus Martinez-Frias and Karoly Nemeth

Received: 29 January 2024
Accepted: 17 February 2024
Published: 23 February 2024



Copyright: © 2024 by the authors. Licensee MDPI, Basel, Switzerland. This article is an open access article distributed under the terms and conditions of the Creative Commons Attribution (CC BY) license (<https://creativecommons.org/licenses/by/4.0/>).

1. Introduction and Setting

The Panarea volcanic complex (PVC) is located in the Aeolian Archipelago, in the southern Tyrrhenian Sea (Figure 1). It includes the Panarea Island, on the western side of the complex, the Basiluzzo Island, to the northeast, and other several islets and reefs located on the center of the main structure [1–3].

The archipelago consists of seven main islands and a few islets, including the active Stromboli and Vulcano [4,5]. It is part of a complex geological context, in which a volcanic arc has been formed by the convergence of the African and Eurasian plates and the subduction and southeastward rollback of the Ionian lithosphere [3,6–13]. This complex geodynamic system results in compression in the eastern sector and in strike-slip faulting and extension in the central and western sectors (Figure 1) [3]. These three structural sectors are: the NE–SW-trending sector, connecting the Panarea and Stromboli islands; the E–W-striking belt, linking Salina Island to Alicudi Island; and the NNW–SSE, central, transverse sector, including the Salina, Lipari and Vulcano islands [1,3]. The current deformation pattern is connected to the NE–SW trending faults of the area [1–4,12,14]. In this complex geodynamic, the Aeolian arc is characterized by a calc-alkaline volcanism superimposed on a sialic basement [3,11,15,16]. The arc formed from 1 to 0 Ma [4], with the volcanic rocks being younger from west to east [13], while the age of the outcropping volcanic rocks ranges from 0.5 Ma to present [3,11,15,16].

The PVC shows a conic shape rising from the sea bottom by a steep slope of about 800 m, terminating with a marine abrasion shelf, as inferred by the border depth, which roughly corresponds the last low seal level depth (120–130 m) [3,4,12,17]. Approximately in the center of the shelf emerges the island of Panarea and the few islets.

The submerged magmatism of the PVC dates back to about 0.8 Ma ago [3], with high-K andesite (0.2 Ma) and rhyolite and basalt (0.01 Ma old) magmatic products [11].

The outcropping volcanic rocks of the PVC consist of two main components: the subaerial shaped dacites and rhyolites and effusive submerged high-K basalts [2–16]. These rocks are located in the central area of the PVC and span from $133,000 \pm 9000$ y to 10,000–20,000 y [2]. The most recent rocks emerge on the rhyolite dome of the Basiluzzo Island (10,000 years old [2,15]) and on the basaltic tuff on the Panarea Island [2–4,16]. Moreover, the subaerial rhyolitic–rhyodacitic rocks outcrop on the eastern side of the Panarea Island. The rhyodacite rocks contain igneous xenoliths, with a basic to intermediate character, as well as HKCA to shoshonitic affinity [3]. A stratigraphic structure of the PVC has been reconstructed by [18]; this is composed of three different lithofacies units: the lower Unit C, formed by highly crystalline andesite lava; the intermediate Unit B, constituted by basaltic–andesite to andesite porphyric lava with xenoliths; and the upper Unit A, including sand and gravel, conglomerate and breccia.

The Aeolian arc and the south-eastern circum-Tyrrhenian area are characterized by intense widespread non-eruptive sub aerial degassing activity at vents along the flanks of active volcanoes. This sub aerial degassing activity releases mainly CO₂ [13]. The volcano and Stromboli emit between 0.06 and 2 Mt/y of CO₂, while the rest of the Tyrrhenian area emits between 6.31 and 20.91 Mt/y of CO₂ of volcanic origin [13]. This CO₂ is produced by the rollback mechanism of the ionic lithospheric, which creates a depression as a consequence of the rising of the mantle; this produces a melting and rising of the carbonates with subsequent migration through faults and leakage of the degassed CO₂ to the surface [13]. The carbonate-enriched melt would have been due to the subduction of carbonate sediment-bearing old oceanic and/or continental Adria lithosphere either by decarbonation or by melting reactions [13].

Around the Panarea Island, gas-charged sediments, diffused hydrothermal activities and vents have been reported and described on the seafloor east and north-east and south-east (on the *Secca dei Pesci*) of Panarea Island [2,4,11,15,16,19–36]. On land and shallow waters, fumaroles and vents are present along the coast of Panarea on Calcara beach, in the north of Panarea, the south of Basiluzzo and the shallow area among the islets Dattilo, Lische, Bottaro and Panarelle (DLBP) (Figure 2) shoal. Notably, the marine area east of

Panarea has been known for its fumarolic activity since historical times [5,19]. In particular, the diffused hydrothermal activity is related to a horst and graben system to the NE area of Panarea, which originated from the transtensional tectonics related to a Plio-Pleistocene regional strike-slip fault system (Figure 1). The western boundary of this graben can be traced up to the area NW of Basiluzzo, whereas its eastern boundary extends to the area SW and NE of Basiluzzo [15].

These hydrothermal activities are associated with sea bed patches of white sulfate [2–4,16] and bacterial mats [37] that are overcomplex and variable from one area to another and in-depth mixtures of low-temperature chemical deposits [3], associated with altered pyroclastites [2–4,11,16,23]. These formations consist of reddish and ochre crusts of iron oxyhydroxides [16] over variable associations of gravel pumice blanket that are ferrous and argillic (quartz, cristobalite, montmorillonite and kaolinite) alterations, metal sulfides (galena, sphalerite or blenda, pyrite and marcasite), barite, massive sulfides (mainly pyrite and sphalerite and galena [16]) and marcasite, alunite and pyrite [4,23]. In particular, massive sulfide deposits are reported on the eastern walls of the depression lying among the Panarea, Basiluzzo and Dattilo Islets and the Panarelle (DLBP) shoal (Figure 2), while massive sulfide deposits enriched in Ba, Pb (Galena) and Zn (Sphalerite) are reported on the south of Basiluzzo Islet, along and near the eastern shelf break [16]. The area with massive sulfide deposits may extend southward to the shallower area of the islets [23].

Ref. [23] pointed out that massive sulfides formed in three stages: in the first, upwelling of a deep, acidic and hot hydrothermal fluid leached metals from the host rocks and then mixed with ambient seawater and precipitated dominantly marcasite; in the second, the increasing seawater proportion in the fluid as well as the exhausted iron content of the hosting rocks promote the alunite precipitation at the seafloor; in the third, a further decrease in the proportion of the hydrothermal end-member fluid resulted only in amorphous silica precipitation.

Moreover, Mn-oxide impregnations and cements of volcanoclastic and carbonate breccias with no detailed descriptions and mineralogical and geochemical data have been reported [11]. Fe-oxyhydroxide-rich sediments, crusts and chimneys are reported on depressions and scarps on the western part of the DLBP shoal, SW of Panarea, NW of Basiluzzo Islet and NE of the Basiluzzo submerged ridge [16].

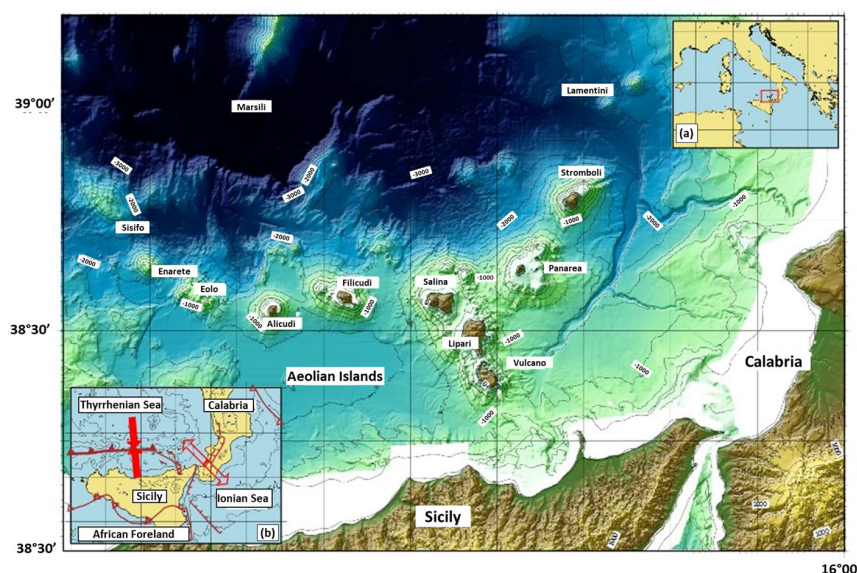


Figure 1. Bathymetry, morphology and tectonic setting of the Aeolian Islands in the Southern Tyrrhenian Sea (modified from [3,16,38,39]). In the insert (a) the red rectangle highlights the area of Figure 1. In box (b), at the bottom left, a summary of the main tectonic structures are drawn after [1].
 —▶▶ Reverse and thrusting compressional areas, ◀◀ normal and extensional area, ▲ thrust, ⇄ strike-slip faults, ||| extensional faults. Depths in meters.

PVC has thoroughly been investigated in the late 1990s by Italian CNR scientists using multibeam sonar systems, side-scan sonars, ROV and bottom sea sampling [2–4,16,20–22,26–30,37–43].

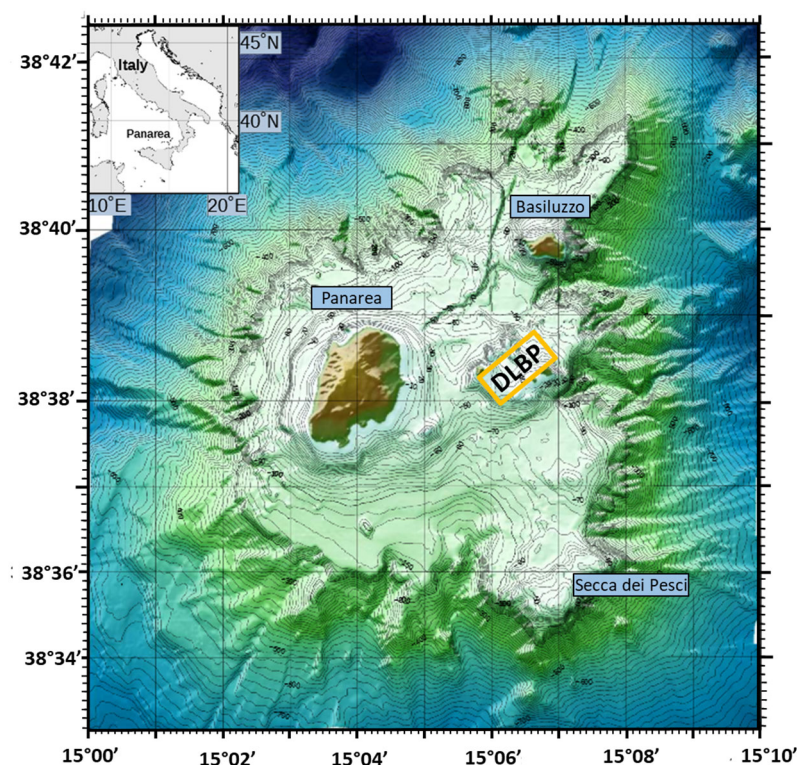


Figure 2. Bathymetries of the Panarea volcanic complex (modified from [20,29,38,39]). DLBP: shallow area among the islets Dattilo, Lische, Bottaro and Panarelle. On-land topography LiDAR data from [44].

The strong interest attracted by the PVC in the past few years is due to a gas burst event which took place to the east of Panarea on the 3 November 2002. After the initial burst, a substantial gas flux continued to be released for years from fractures and sinkholes on the seafloor, mostly near Bottaro Islet [18,20,26,27,31,34].

Geological and oceanographic investigations between Panarea and Bottaro began immediately after the burst to determine its geological and geochemical origin and features, its possible connection with regional tectonics and its hydrothermal or magmatic nature [45–49], as well as to perform volcanological surveillance and risk assessments [21,22].

The burst event was first evidenced by substantial columns of bubbles rising from the seafloor to the surface. Subsequently, several active spots were identified by divers, ROVs and multibeam surveys [18,20,21,26,28]. At this time, the most remarkable vent (*Punto Emissione Gas 1*: PEG1) was just SW of Bottaro (Figure 3a). Here, gas leaked from an elliptical depression produced by the explosive collapse of the seafloor and reached the surface from a depth of 15 m; a sediment plume was also detected on the surface for several days [18,21,26].

During the most active degassing period, from the burst up to mid-2003, the emissions consisted of a CO₂-dominated gas phase emulsion with suspended sediments and colloidal sulfur; the water was acidified by the dissolution of SO₂, HCl and HF [31,32]. By 2006 and 2007, the gas fluxes had visibly shrunk to a small area [26]. Other authors reported data about the composition of submarine gas venting from the PVC bottom in different times and areas, always resulting in a prevalence of CO₂: CO₂ with minor HCl, HF, SO₂ and H₂S, traces of S, N₂, CH₄, Ar, O₂, Ne, H₂, He, CO and C₂H₆ [32], dominating CO₂ and minor (1–4%) H₂S [2,16] and mainly CO₂ (96.6–98.6 vol.%) [34,47].

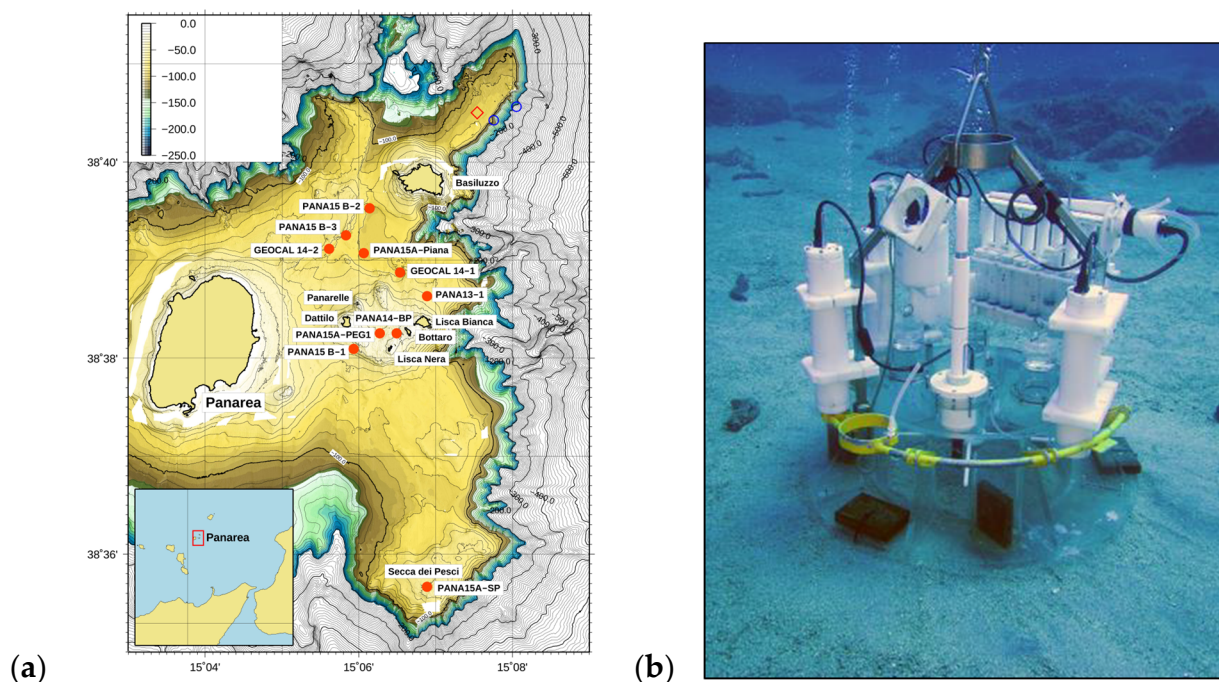


Figure 3. (a) Positioning of the AdaN stations on the seafloor to the NE and SE of Panarea (modified from [39,43]). The PEG1 (*Punto Emissione Gas 1*), which is the site of the 2002 burst, is in correspondence of the PANA15A-PEG1 incubation site. (b). AdaN benthic chamber deployed on the PVC sea bottom.

With regard to the quantification of the venting, Caliro et al. [47] estimated that the gas output was 10^9 L/d (November 2002) and 2 to 4×10^7 L/d (from May to July 2003), which are orders of magnitude higher than the total gas output of 10^6 L/d, measured in the islets in the 1980s [18]. A study of the water fluxes at PEG1 [20] also estimated that in December 2002 and September 2003, the gas fluxes were, respectively, 2.6×10^8 and 0.3×10^8 L/d. Based on the data available at the time, [34] calculated that ~ 70 Mt of CO_2 would have been emitted in the area in the past 10,000 years.

Notably, the acid plumes have affected the marine environment, inducing changes in the biota [35,39] and in water properties [36].

In this paper, we present, for the first time, a direct in situ quantification of bottom sea hydrothermal fluid and ion seeps as well as the results of the morphological and geochemical investigations carried out in the course of several oceanographic cruises in order to characterize the PVC, its hydrothermal activity and its geological setting. Particularly, the new data allow for highlighting the contribution of the active submerged marine volcanic area to the global marine CO_2 budget and, consequently, to the ocean acidification that is the global change. This work allowed us to characterize the hydrothermal ecosystems and the tectonic structures of the upper PVC through a multidisciplinary approach combining the analysis of submerged morphology, dissolved benthic fluxes, water column shelf hydrology and hydrobiogeochemical data.

2. Materials and Methods

Bathymetric and morphological reconstruction and interpretations are based on the data collected by multibeam sonar systems in previous oceanographic cruises and research [2–4,16,18,20–22,26,40–42] as well as in cruises from 2013 to 2015 [39,43]. Previous and 2013–2015 acoustic investigations allowed for mapping almost the entire PVC bottom sea (Figures 1 and 2). The great mass and high-quality acoustic data allowed for the production of high-definition bathymetry maps of the PVC bottom sea shelf, providing a very detailed geomorphology of the plateau created during the last low stand sea level [17] (Figures 2 and 3). This allowed for a better definition and identification of new tectonic

structures on the NE of Panarea, as well as gas vent morphologies that had already been partially described in earlier papers [2,4,15,16,18,20,22,25,26,29,30,34].

Dissolved Inorganic Carbon (DIC) and dissolved metal fluxes at the sediment–water interface (Dissolved Benthic Fluxes: DBFs) were measured in the oceanographic cruises carried out from 2013 to 2015 to explore the hydrothermal processes of the PVC, to quantify the release of fluids and gases from the volcanic sea bottom and to gain insights into the global marine CO₂ cycle and the marine CO₂ budget, as well as the contribution of submarine volcanic degassing to ocean acidification. DBFs were measured in situ by the AdaN (Figure 3a), an automated benthic chamber whose details and functioning are described in [50,51]. It must be specified that, due to its technical characteristics, a benthic chamber is able to measure the diffusive or punctual fluxes of fluids coming from the seabed, while it cannot measure the gas fluxes in gaseous form unless these are reabsorbed by the solution during the measurement. The deployment of a benthic chamber requires good knowledge of bottom topography and sediment features, because it needs a flat area with fairly soft sediment to achieve the bottom sealing of the chamber and obtain accurate flux data. Extensive multibeam swath bathymetry, ROV dives and core sediment sampling in the PVC allowed for identifying safe and suitable deployment sites.

From 2013 to 2015, AdaN was deployed at 10 sites (Table 1, Figure 3). The depth data recorded by the multiparameter probe allowed us to precisely determine the chamber bottoming and surfacing, which mark the beginning and end of the incubation, as well as the depth variations due to tides and wave motions. The beginning and end of the incubation were marked by stable depth readings (Figure 4a, see below for an explanation of deployment at PANA14-BP). On the whole, the range variations between high and low tide were 10–20 cm, whereas the depth differences due to wave motion were in the order of a few centimeters (Table 1).

Table 1. Location and statistical data of the AdaN benthic chamber deployments. PANA14-BP = Black Point crater, PEG1 = *Punto Emissione Gas 1*, SP = *Secca dei Pesci*. (a) Tidal ranges: difference between the maximum and minimum depth recorded by the AdaN pressure probe during deployment; (b) Wave ranges: absolute value of the difference between two successive measurements of the pressure probe in a deployment ($|x| = x_{n+1} - x_n$).

Cruises	Stations	Date	Longitude	Latitude	Incubation Time (h)	Max Depth (m)	Min Depth (m)	Average (cm)	a (m)	b (m)
PANA13	PANA13-1	5 June 2013	38°38.592'	15°06.901'	8.25	40.3	40.12	40.20	0.18	0.06
GEOCAL14	GEOCAL14-1	6 May 2014	38°38.930'	15°06.501'	9.17	80.4	80.28	80.35	0.12	0.02
GEOCAL14	GEOCAL14-2	6 May 2014	38°39.098'	15°05.596'	10.58	76.03	75.84	75.95	0.19	0.03
PANA14	PANA14-BP	7 July 2014	38°38.243'	15°06.292'	4.13	23.24	23.17	23.21	0.07	1.09
PANA15A	PANA15A-Piana	10 June 2015	38°39.088'	15°06.124'	6.33	82.18	82.05	82.09	0.13	0.03
PANA15A	PANA15A-PEG1	9 June 2015	38°38.246'	15°06.564'	6.25	11.63	11.43	11.54	0.20	0.04
PANA15A	PANA15A-SP	8 June 2015	38°35.668'	15°06.930'	9.51	38.46	38.29	38.40	0.17	0.02
PANA15B	PANA15B-1	26 June 2015	38°38.163'	15°05.927'	6.33	59.5	59.39	59.47	0.11	0.02
PANA15B	PANA15B-2	28 June 2015	38°39.538'	15°06.146'	5.50	84.44	84.34	84.38	0.10	0.02
PANA15B	PANA15B-3	29 June 2015	38°39.265'	15°05.911'	4.95	71.72	71.64	71.68	0.08	0.34

The first deployment (PANA13-1, Figure 3b) was on 5 June 2013, from the hydrographic vessel “*Ammiraglio Magnaghi*” of the Italian Navy. At this station, the AdaN was deployed at a depth of 40.3 m for 8.25 h [39]. The second and third deployments (GEOCAL14-1 and GEOCAL14-2) were on 6 May 2014, from the CNR R/V “*Urania*” during the GEO-CAL 2014 cruise [43]. During this cruise the AdaN was deployed at 80.4 m for 9.17 h (GEOCAL14-1) and at 76.03 m for 10.58 h (GEOCAL14-2). All subsequent deployments were from the ISPRA R/V “*Astrea*”. On 7 July 2014, the chamber was deployed at the Black Point (Figures 3 and 4) at a depth of 23.24 m for 4.13 h. The Black Point is a crater-like structure that, in the few first months after the 2002 burst, was a black smoker. Later, in 2014, it was venting almost diffusively from a flat bottom and was characterized by a black precipitate around a vent discharging hot, low-pH water fluids and gases [18,20]. Deploying the chamber into the Black Point crater involved some difficulties (Figure 4), since at the first site, a boulder prevented sealing, requiring the divers to move the AdaN to a nearby site (Figure 4b). The moving is clearly reflected in the depth and temperature data

(Figure 4a, black and red lines). The depth profile clearly shows the time of the first, failed deployment of the chamber, its displacement, marked by a sudden depth reduction at 16:58:00, and, finally, its final recovery. During the move, the water temperature decreased due to the entry of seawater. From 8 to 10 June 2015, during the PANA15A cruise, the AdaN was deployed three times at: (i) PANA15A-SP (*Secca dei Pesci*), at 38.4 m for 9.51 h; (ii) PANA15A-PEG1, at 11.63 m for 6.25 h; and (iii) PANA15A-Piana, at 82.18 m for 6.33 h. Finally, from 28 to 26 June 2015, during the PANA15B cruise, the AdaN was deployed at three other stations: (i) PANA15B-1, at 59.5 m for 4.92 h; (ii) PANA15B-2, at 84.44 m for 5.50 h; and (iii) PANA15B-3, at a depth of 71.72 m for 4.95 h (Figure 3). At PANA15B-1, a technical problem due to the failure of the probe batteries prevented the recording of the final part of the experiment; however, the extant recording allowed for recognizing the general trend of the parameters.

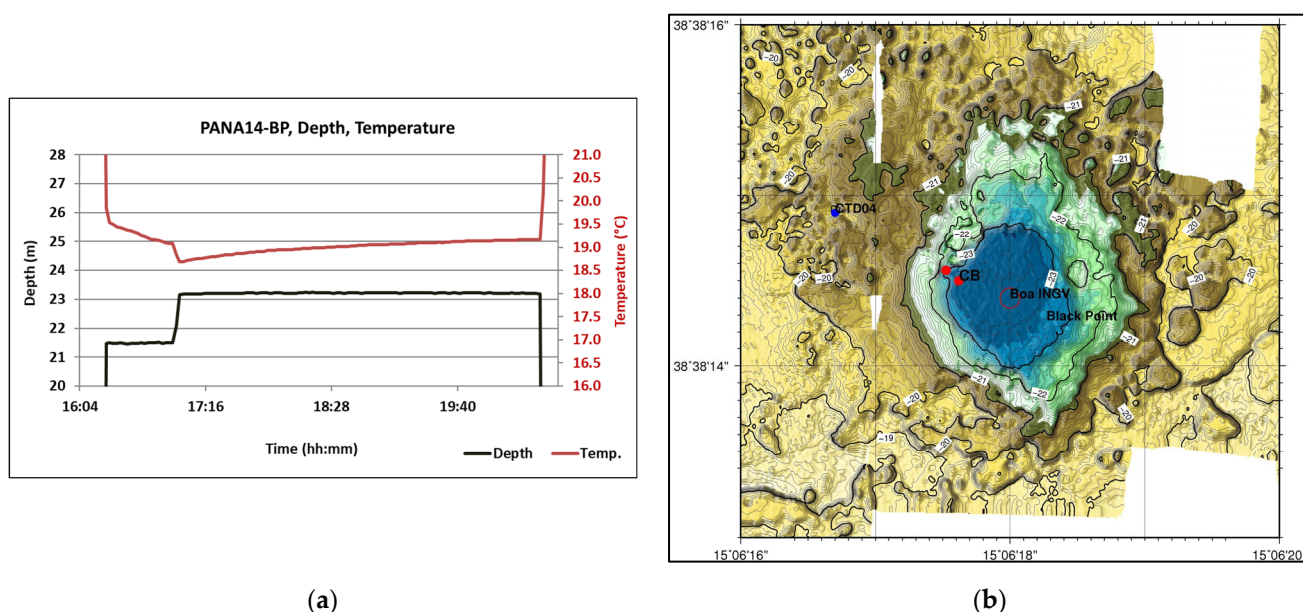


Figure 4. Deployment of the benthic chamber at the Black Point (PANA14-BP). (a) Depth and physicochemical parameters recorded at the PANA14-BP station by the multiparametric probe mounted in the AdaN: the depth data (black line) mark the start and end of the incubation experiment as well as the depth changing subsequent to the move; the salinity recording also marks the input of seawater due to the moving; (b) Black Point crater. Detailed morphology of the area with location of the two AdaN deployment sites (red dots), of a CTD cast (blue dot) and site of the INGV monitoring buoy (red circle).

The DBFs of oxygen, DIC, metals (Fe, Mn, Zn, Al, Ni and B) and protons were measured. Other gases were not analyzed because of their scarce presence in the gas exhalation of the submarine bottom of PVC [2,16,32,34,47].

Oxygen and pH DBFs were determined using the concentration measured by the multiparametric probe inside the chamber during the incubations, while DIC and metal DBFs were calculated by the concentrations measured in the water samples collected in the chamber. The DIC concentrations were measured by a modified Coulometric method [52], whereas the metal concentrations were analyzed by ICP-OES.

When the DBF values were very small such that the total error, due to the measurement and straight-line fitting (R^2), was higher than the concentration changes over time, they were considered non-measurable and assumed to be zero ($\sim 0 \text{ mmol} \cdot \text{m}^{-2} \cdot \text{d}^{-1}$).

Metals, mainly Fe and Mn, were analyzed only at some stations. Individual element concentrations were not determined at stations where the fluxes were considered zero (PANA15A-Piana, PANA15B-2 and PANA15B-3), nor at stations PANA14-1 and PANA15A-peg-1 for the spoiling of the samples.

DIC was analyzed in water column samples collected using either Niskin bottles mounted on a rosette sampler or a syringe, on board, in the water overlaying the sediment collected by the box-corer.

The fluxes at the sediment–water interface were calculated as follows:

$$J_i = \frac{C_{i*}}{d_t} * V \quad (1)$$

where: J_i is the flux of chemical i , in mol (or millimoles or micromoles, depending on the chemical)·m⁻²·d⁻¹ (d = days), C_i is the concentration of chemical i at time t in the chamber and V is the chamber volume.

The application of (1) resolves as follows:

$$J_i = m_i \quad (2)$$

where m_i is the slope of the straight line, calculated by the least square's method in a graph with time on the x -axis and $C_i \cdot h$ on the y -axis, with h being the height of the benthic chamber.

Regarding the water column, Oxygen, pH and pCO₂ as well as methane in limited stations were measured by CTD casts (*SBE 19plus* and *SBE 9* probes (Sea-Bird Scientific, Bellevue, WA, USA) equipped with O₂, pH, pCO₂ and CH₄ sensors) and by a multiparametric probe (*Hydrolab MS5* (Aqualab Scientific Pty Limited, Villiers Place, Australia)) equipped with pH and O₂ sensors) and a pCO₂ sensor installed on the ROV frame (*POLLUX III*, *Stella Di Mare s.r.l.*, Livorno, Italy).

CTD casts were collected in various cruises, but only the CTD casts obtained from the 2014 cruise GEOCAL14 [43] and located on the north of the DLBP (Figure 5) are discussed here.

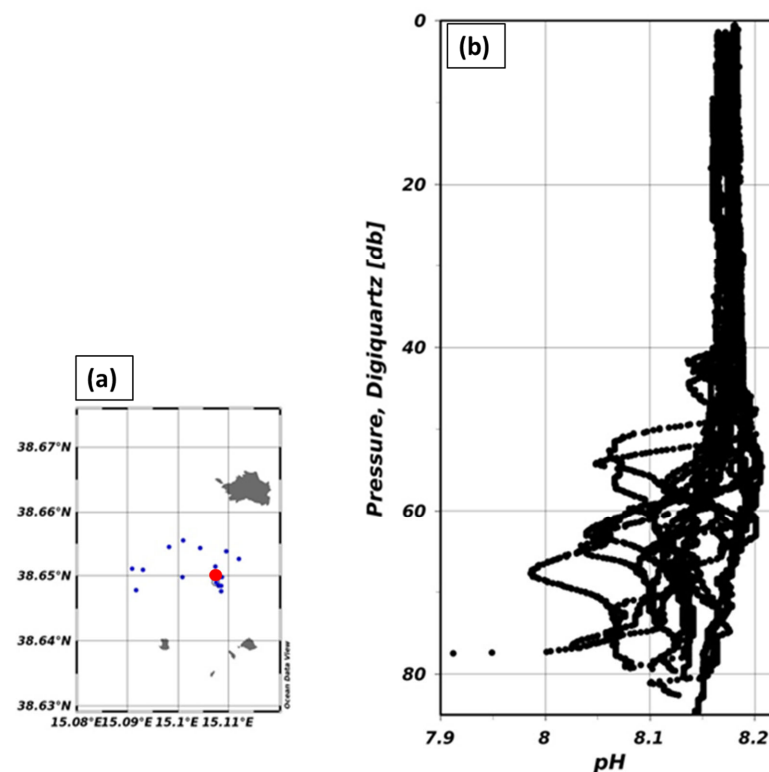


Figure 5. (a) Location of the CTD casts in the GEOCAL14 Cruise (blue and red dots), red dot: P007 CTD station; (b) pH water column profiles from the GEOCAL14 Cruise [28].

The ROV was used as well to select suitable sites for chamber deployment, to directly identify and observe the vents and any morphological structures such as chimneys, cones and craters and to measure pCO₂ near and just above the venting sites.

Finally, some crust samples collected by ROV or subsampled in the box-corer have been analyzed regarding the elemental composition by XRF (ESEM Zeiss EVO LS 10 with a thermo-ionic source (LaB₆) (Carl Zeiss AG, Jena, Germany) coupled with the EDS *Quantax* (Bruker S8, Billerica, MA, USA) with SDD, courtesy of the CNR-IMM (Bologna, Italy)).

3. Results

3.1. Bathymetric Investigations

The detailed geophysical exploration of the area between Panarea and Basiluzzo allowed us to define the morphological details of the depression bordered, on the NW, by SW-NE escarpments of variable heights and directions and, on the SE, by a corrugated relief with numerous scattered craters as well as escarpments showing a varying degree of elongation (Figure 6). This depression has been called, for the first time in this paper, Smoking Land Valley (SLV), to recall the “Smoking Land” present at the base of the northern border of the SLV (Figure 7) and discovered as well as called for the first time by [22]. In the Smoking Land area, more than 200 active and relict chimneys up to three meters high are grouped in an elongated field at the base of the northwestern slope [22]. Instead, on the southern border of the SLV, several sub-circular depressions and craters measuring some meters are localized among the islets, on the DLBP shoal and on the east of the southeastern slope of the SLV depression (Figure 6b–d). The craters are generally filled with gravel or sandy material [20] and are either currently inactive or show a weak releasing activity [22,39,43]. This area has been called Panarea Moon Land (PML) to recall the particular landscape of our satellite (Figure 6c).

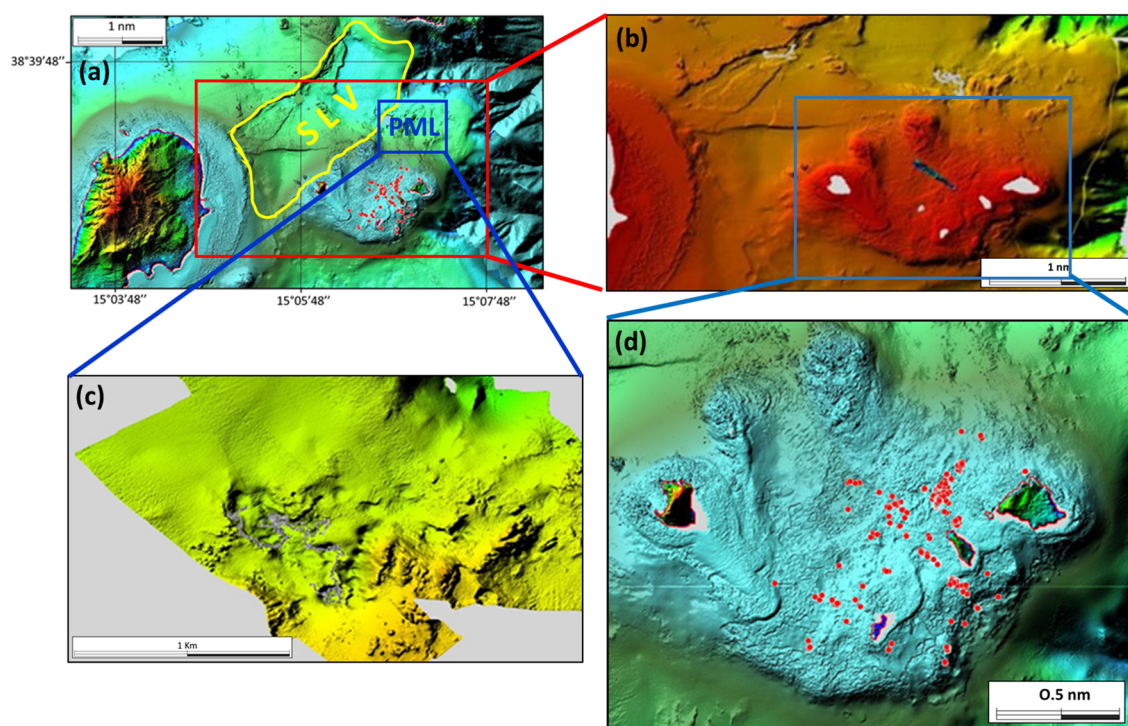


Figure 6. Areas mapped on the NE of the Panarea volcanic complex after the 2013–2015 cruises [28,30,39,43]. (a) Area to the E and NE of Panarea showing the: SLV (Yellow line) depression stretching SW-NE, bordered by the high and steep escarpment to the NW and by the corrugated relief to the SE (in this last area, numerous crater-like structures are also visible); PML area (red rectangle); (b) zoom on the SLV and DLBP areas; (c) zoom on the PML area; (d) zoom on the southeastern border of the SLV (after [18,20,28], highlighting the multi-crater pattern morphology and the main active degassing points) (red dots) identified by multibeam, divers and ROV [18,21,26,28]). On-land topography LiDAR data from [44]. Red triangle: the PML: Panarea Moon Land; yellow closed line: SLV: Smoking Land Valley (see the explication in the text for the meaning).

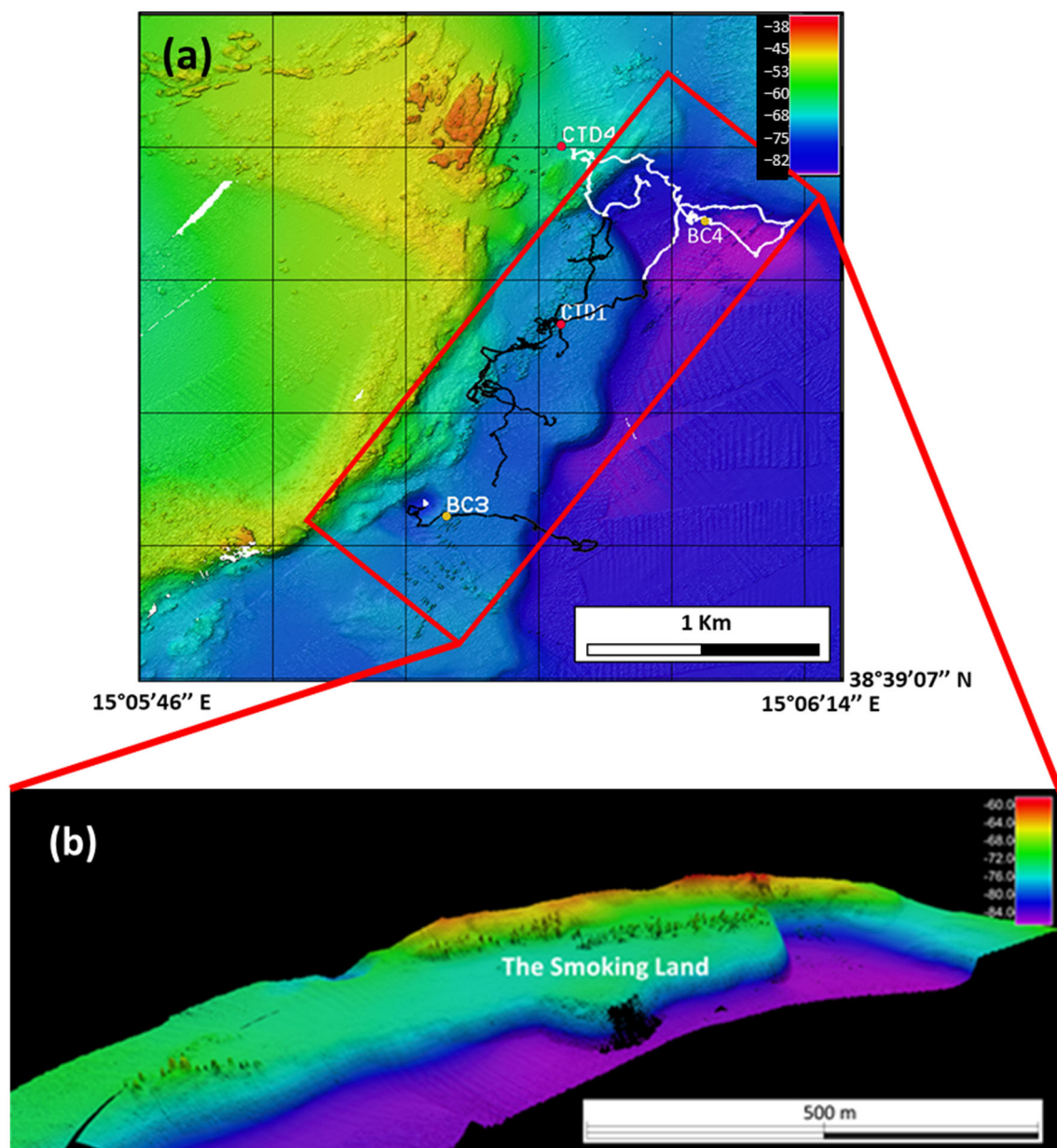


Figure 7. Areas mapped on the NE of the Panarea volcanic complex after the 2013–2015 cruises [28–30,39,43]. (a) Particular of the high and steep slope on the northwestern border of the SLV with the Smoking Land and the traces of the ROV dives; (b) Bird-view zoom of the Smoking Land with the 200 active and relict chimneys (from [22]).

Furthermore, the detailed geophysical exploration on the ridge to the NE of Basiluzzo Islet allowed for the individuation of pinnacles of different sizes (Figure 8). In this area, the pinnacles are scattered inactively [29].

In the area to the south and SE of Panarea, the multibeam and ROV investigations allowed us to highlight an area characterized by a flat bottom shaped during the last low stand sea level interrupted by higher and irregular structures (Figure 9a). On the southeastern part of the PVC, another venting area at 38 m, just north of the summit of the *Secca dei Pesci* shoal (at the top at a depth of 33 m), has been individuated (Figure 9b). This is characterized by a sub-circular depression with a sandy bottom and sediment dunes created by bottom currents. Furthermore, gas venting was detected on a depression at a depth of 80 m, to the north of the shoal, and on the shoal itself.

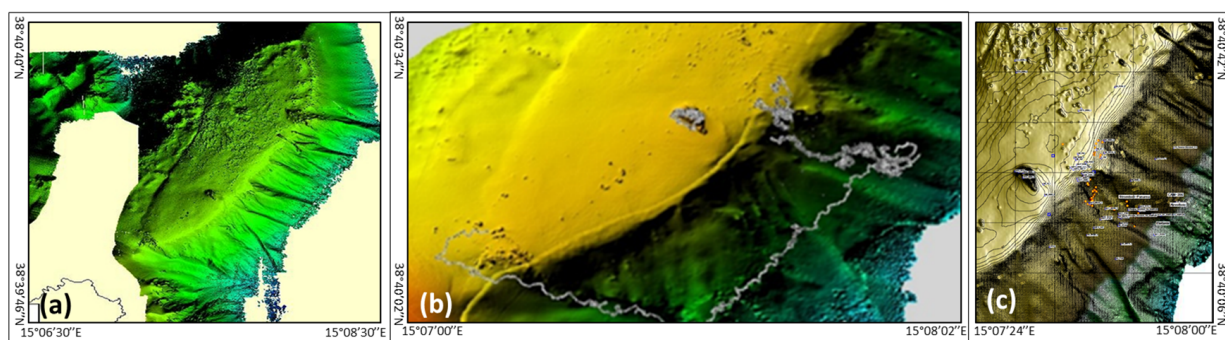


Figure 8. Areas mapped on the ridge to the NE of Basiluzzo after the 2013–2015 cruises [28–30,39,43]. (a) Morphology of the ridge to the NE of Basiluzzo Islet (from [28,29]), with scattered pinnacles identified as relict hydrothermal chimneys [29]; (b) zoom on the Basiluzzo NE ridge showing the presence of scattered chimneys; greater zoom on the Basiluzzo NE ridge showing the location of the relict chimney; (c) zoom on the NE side of the Basiluzzo ridge showing the sites of relict chimneys identified by ROV dives on the eastern flank.

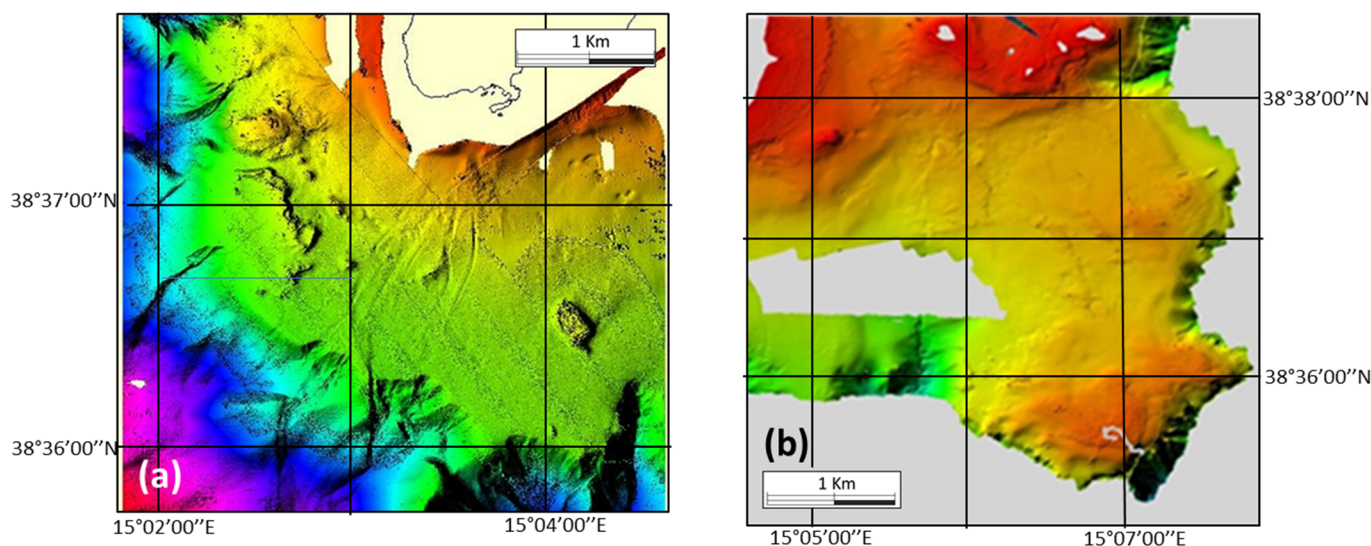


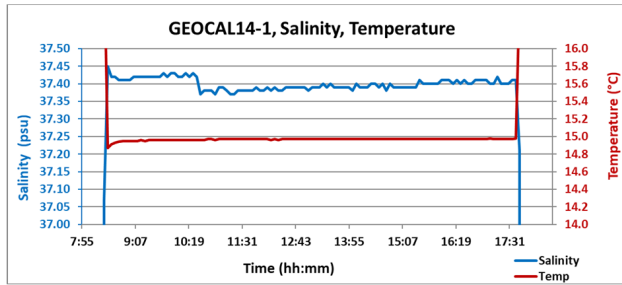
Figure 9. Areas mapped on the south and SE of the Panarea volcanic complex after the 2013–2015 cruises [28,30,39,43]. (a) Area to the S of Panarea; (b) area of the *Secca dei Pesci* (grey line: trace of the ROV dive on the *Secca dei Pesci*) [28].

3.2. Flux Estimation and Oceanographic Data

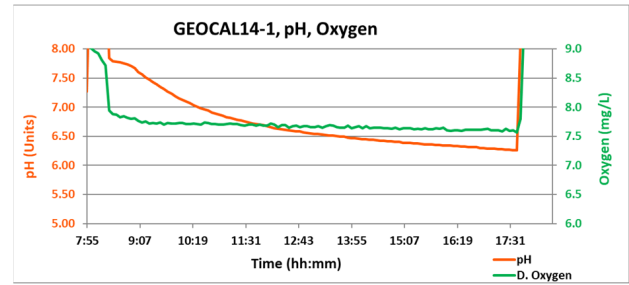
3.2.1. Physicochemical Parameters Measured in the AdaN Benthic Chamber

The physicochemical parameters measured by AdaN allow for grouping the stations into two main cluster (see Figure 3 and Table 1 for their location). The first cluster (Figure 10) includes stations with appreciable (>0 , see Section 2 for >0 definition) variations in pH and oxygen concentrations during the incubation (PANA13-1, GEOCAL14-1, GEOCAL14-2, PANA14-BP, PANA15A-SP and PANA15A-PEG1), whereas the second cluster (Figure 11) includes stations where the physicochemical parameters showed no appreciable (~ 0) variations (PANA15A-Piana, PANA15B-1, PANA15B-2 and PANA15B-3). In the first group, GEOCAL14-1, GEOCAL14-2 and PANA14-BP were characterized by a constant temperature and salinity and by a steep reduction in pH and oxygen (Figure 10a–f). These patterns identify the release of acidic and anoxic fluids from the sea bottom, their oxidation by the oxygen present in the water inside the chamber and a proton increase. However, in this first group, the stations PANA13-1 and PANA15A-PEG1 (Figure 10g–j) were characterized by temperature fluctuations, slight declines in salinity and irregular oxygen and pH trends,

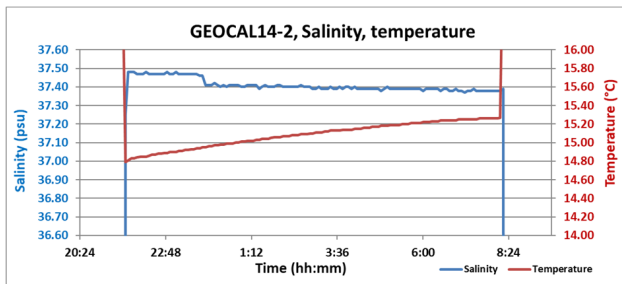
with steeper declines and slower rises. This suggests the release of acidic, anoxic and slightly saline fluids, similar to the other stations of this group, but also a fluid leaking from the chamber base due to deficient sealing. In addition, at PANA14-BP, the pH (Figure 10f) at the start of the incubation was lower than the usual seawater pH (~6.5, instead of 8.2), suggesting that the seawater near the bottom was acidified by fluid seepages. Finally, in the first group, the station PANA15A-SP (Figure 10k,l) was characterized by marked pH and oxygen decreases as well as by a slight decline in salinity, albeit without the steep fall due to the injection of CsCl solution. Here, we also recorded a seepage of acidic and reduced fluids, as well as a slight leak from the chamber base.



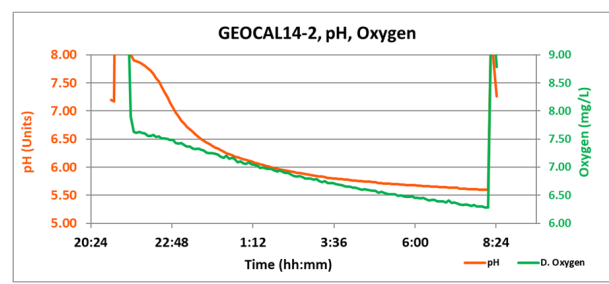
(a)



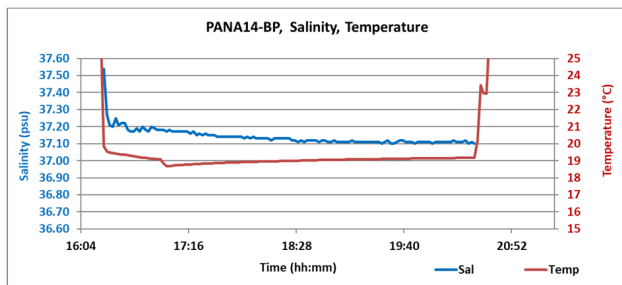
(b)



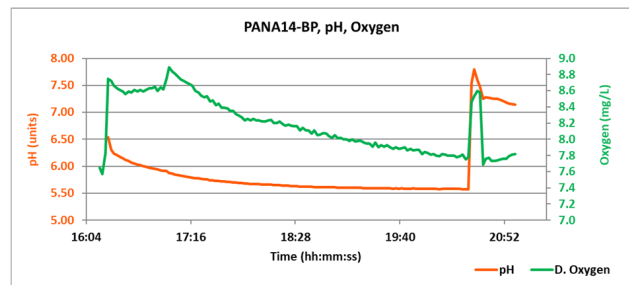
(c)



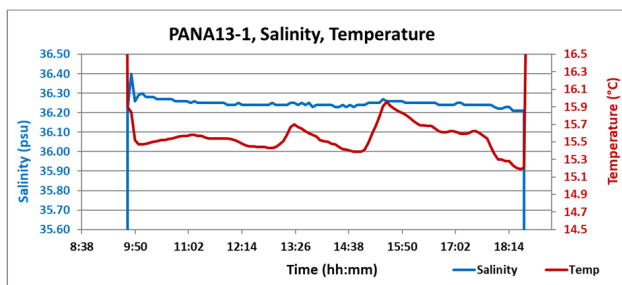
(d)



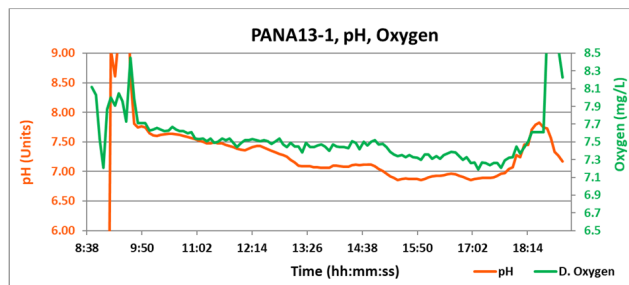
(e)



(f)



(g)



(h)

Figure 10. Cont.

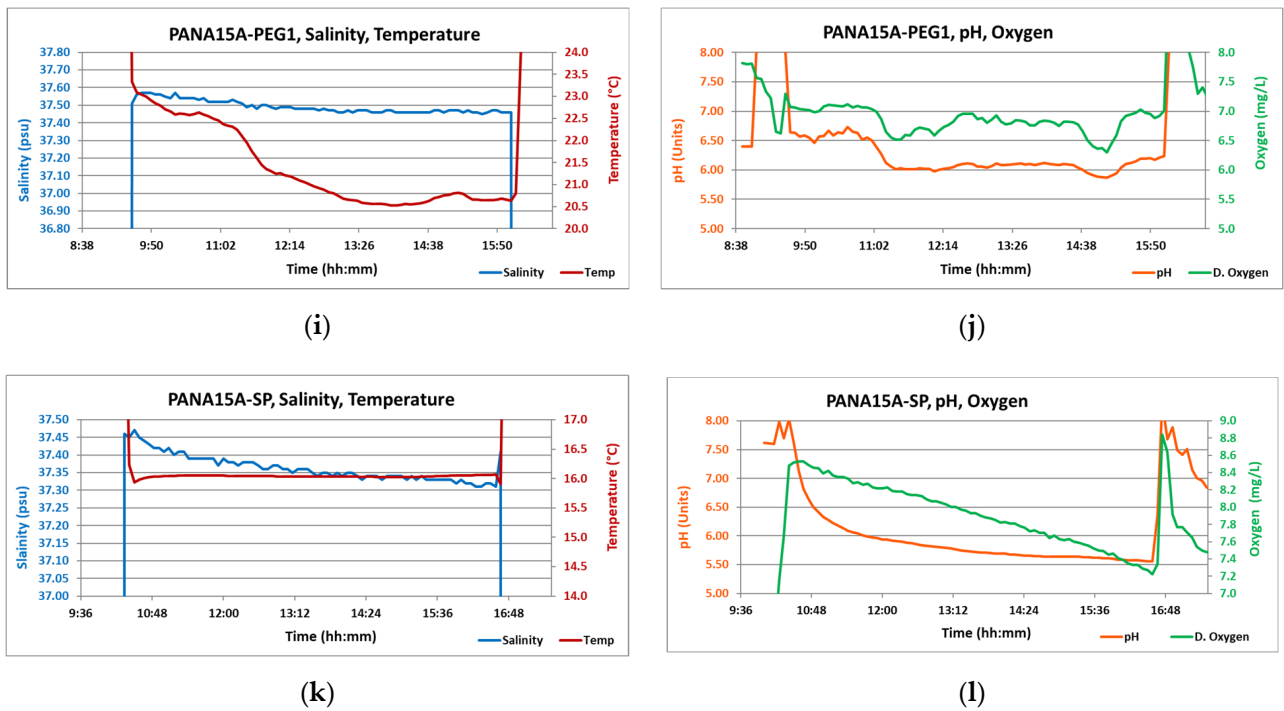


Figure 10. Physicochemical parameters (salinity, temperature, pH and oxygen) measured in the benthic chamber by the *Hydrolab MS5* (Aqualab Scientific Pty Limited, Villiers Place, Australia) probe. The stations GEOCAL 14-1 (a,b), GEOCAL 14-2 (c,d), PANA14-BP (e,f), PANA13-1 (g,h), PANA15A-SP (i,j) and PANA15A-PEG1 (k,l). In GEOCAL 14 stations, the visible salinity step is due to the injection of deionized water.

The second group (Figure 11) includes stations where the values of the physicochemical parameters were almost constant throughout the incubation. The constant values of the physicochemical parameters indicate the absence of fluid seepage.

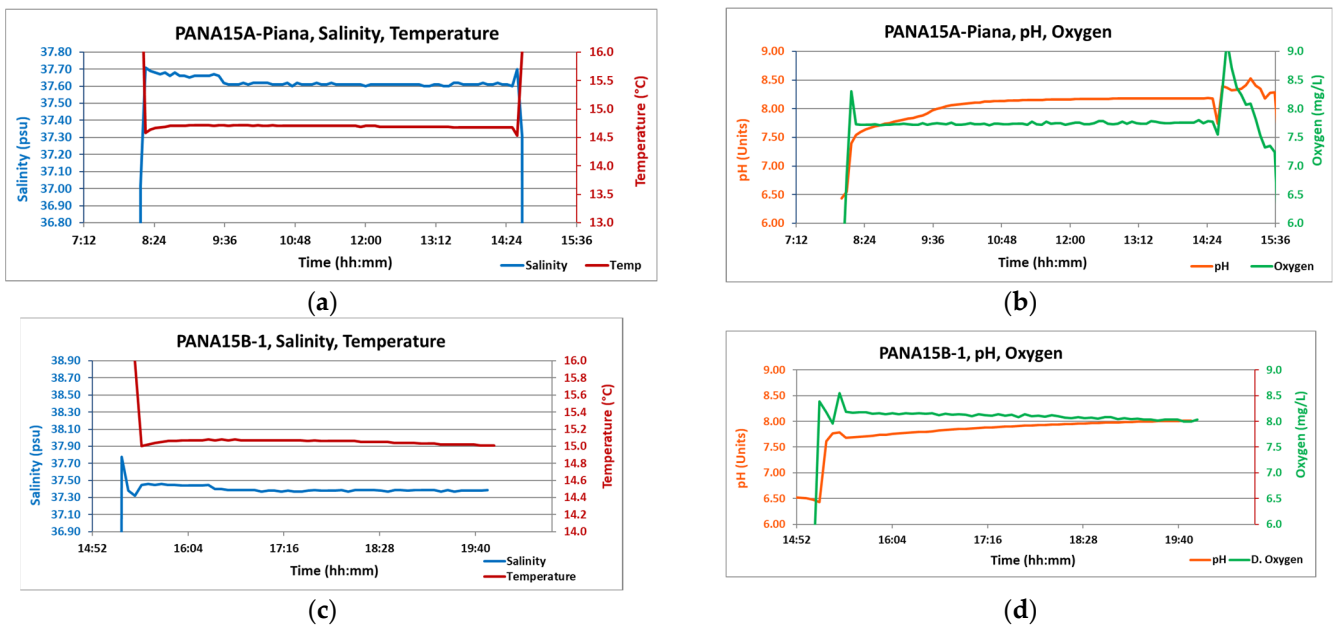


Figure 11. Cont.

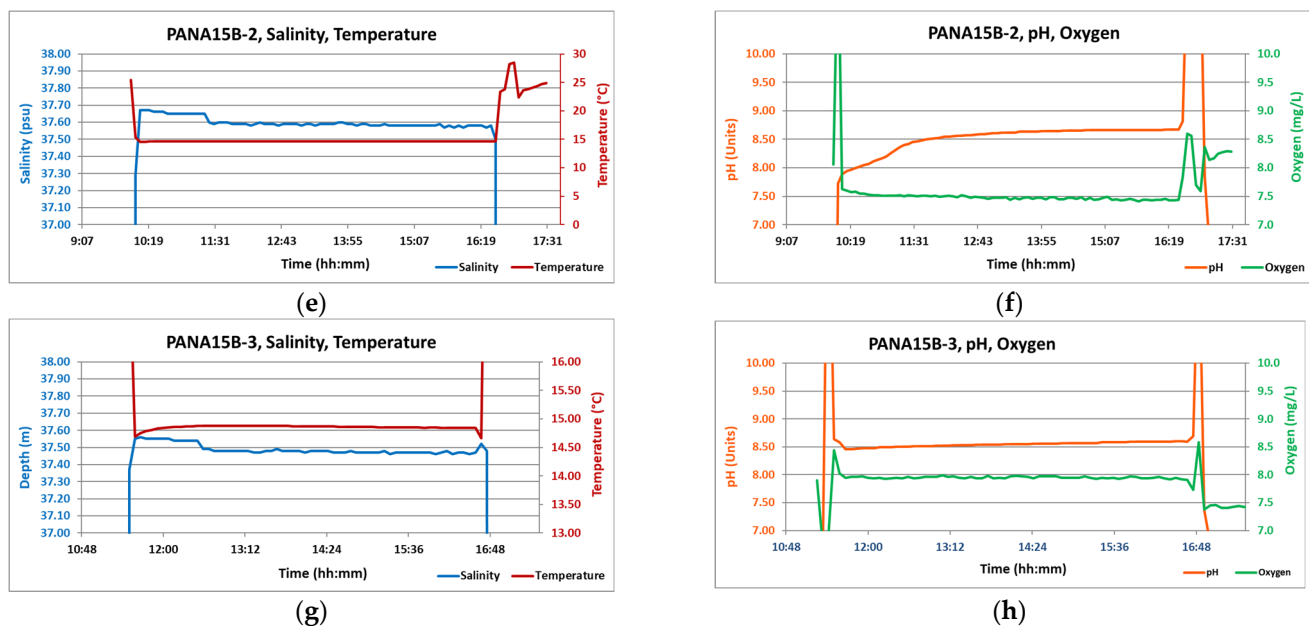


Figure 11. Physicochemical parameters (salinity, temperature, pH and oxygen) measured in the benthic chamber by the *Hydrolab MS5* (Aqualab Scientific Pty Limited, Villiers Place, Australia) probe. Stations PANA15A-Piana (a,b), PANA15B-1 (c,d), PANA15B-2 (e,f) and PANA15B-3 (g,h). Salinity showed the step due to the injection of deionized water, whereas pH sometimes showed a slight initial increase due to sensor stabilization.

3.2.2. Dissolved Fluxes at the Sediment–Water Interface Measured by AdaN

DIC. The DIC fluxes at the sediment–water interface varied widely among the stations (range between 0 and $\sim 11,000 \text{ mmol}\cdot\text{m}^{-2}\cdot\text{d}^{-1}$ (Table 2, Figure 12)). The DIC fluxes at PANA15A-Piana, PANA15B-2 and PANA15B-3 were zero (Table 2, grey rows), owing to the seepage absence. Such stations occur SE of Basiluzzo, in the central flat zone of the SLV (Figures 3b and 6a). Consistent DIC fluxes were recorded at the GEOCAL14-2 station, to the NW of the SLV ($3224 \text{ mmol}\cdot\text{m}^{-2}\cdot\text{d}^{-1}$), and at the PANA13-1, GEOCAL14-1, PANA14-BP, PANA15A-PEG1 and PANA15B-1 stations to the SE of the SLV (Table 2, Figure 12) (range between $61 \text{ mmol}\cdot\text{m}^{-2}\cdot\text{d}^{-1}$ and $2888.9 \text{ mmol}\cdot\text{m}^{-2}\cdot\text{d}^{-1}$). The fluxes were the highest ($11,000 \text{ mmol}\cdot\text{m}^{-2}\cdot\text{d}^{-1}$) on the *Secca dei Pesci* site, at a considerable distance (5 nm) from the SLV (Table 2, Figure 12).

Table 2. Benthic DIC fluxes measured around the Panarea volcanic complex compared with those measured in front of the Po River (Adriatic Sea). R^2 in bold highlights low, hence unreliable, values (flux $\sim 0 \text{ mmol}\cdot\text{m}^{-2}\cdot\text{d}^{-1}$).

#	Cruises	Stations	Flux ($\text{mmol}\cdot\text{m}^{-2}\cdot\text{d}^{-1}$)	R^2
1	PANA13	PANA13–1	60.60	1
2	GEOCAL14	GEOCAL14–1	689.30	0.9872
3	GEOCAL14	GEOCAL14–2	3223.90	0.9514
4	PANA14	PANA14–BP	2888.9	0.9857
5	PANA15A	PANA15A–Piana	–17.988	0.0219
6	PANA15A	PANA15A–PEG1	2750.60	0.9203
7	PANA15A	PANA15A–SP	10,978.00	0.9573
8	PANA15B	PANA15B–1	61.54	0.8165
9	PANA15B	PANA15B–2	–4.4149	0.0014
10	PANA15B	PANA15B–3	–19.29	0.0237
		Average	2950.41	0.67
		Standard deviation	3794.07	0.45
		Po River Prodelta average	29.00	

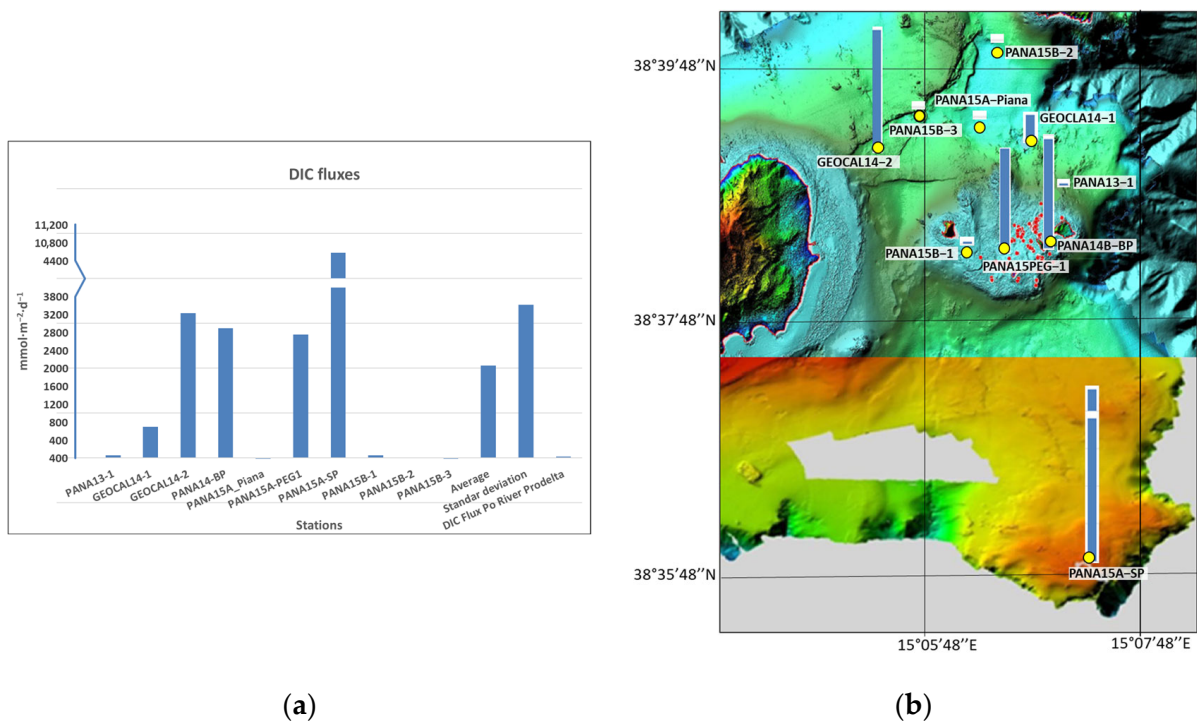


Figure 12. (a) Graph of the DIC fluxes measured at the sediment–water interface around the PVC; (b) Location and graphical view of the DIC fluxes in the SLV and *Secca dei Pesci*.

pH. The dissolved benthic fluxes relative to protons were presented in three ways: as the pH unit increment *per* unit time (units·d⁻¹); as the [H⁺] increment *per* unit area and unit time (mmol·m⁻²·d⁻¹); and as the pH increment *per* unit area and unit time (units·m⁻²·d⁻¹) (Table 3, Figure 13). Like DIC, pH showed proton fluxes equal to 0 at the stations PANA15-Piana, PANA15B-2 and PANA15B-3 (grey rows in Table 3), while at the stations bordering the SLV (PANA13-1, GEOCAL14-1, GEOCAL14-2, PANA14-BP, PANA15A-PEG1 and PANA15B-1), the pH decreased as the [H⁺] rose steeply, indicating a strong proton release from the bottom. As in the case of DIC, the highest proton fluxes were measured at the *Secca dei Pesci*.

Table 3. Dissolved benthic fluxes of pH measured around the PVC.

#	Stations	pH	R ²	[H ⁺]	R ²	pH	R ²
		units·d ⁻¹		mmol·m ⁻² ·d ⁻¹		units·m ⁻² ·d ⁻¹	
1	PANA13-1	-2.6314	0.8882	0.106	0.9021	-0.7105	0.8882
2	GEOCAL14-1	-3.1246	0.8494	0.505	0.9968	-0.9531	0.8401
3	GEOCAL14-2	-3.8024	0.7331	1.754	0.9902	-1.0267	0.7331
4	PANA14-BP	-1.6992	0.8174	2.237	0.8695	-0.4588	0.8174
5	PANA15A-Piana	0.44	0.8043	-0.0019355	0.7838	0.118	0.8043
6	PANA15A-PEG1 average	-1.9987	0.4405	0.651	0.3816	-0.5397	0.4405
7	PANA15A-SP	-3.4737	0.7069	2.624	0.9581	-0.9379	0.7069
8	PANA15B-1	1.82	0.9620	-0.01543	0.9148	0.493	0.9620
9	PANA15B-2	1.25	0.6781	-0.00238	0.5510	0.337	0.6781
10	PANA15B-3	0.63	0.9677	-0.00114	0.9527	0.171	0.9677
	Average	1.04		1.313		0.280	
	Standard deviation	0.63		1.031		0.170	

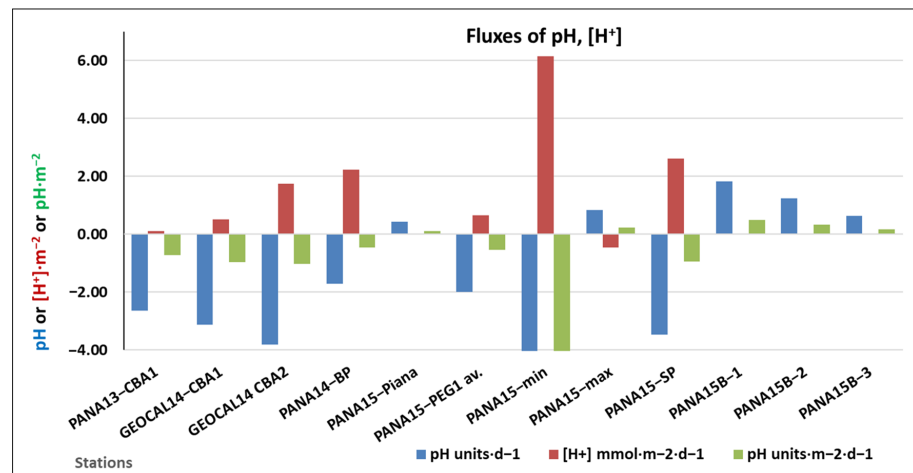


Figure 13. Graph of pH fluxes at the sediment–water interface, measured around the PVC.

Oxygen. Oxygen fluxes were negative (Table 4, Figure 14) in the stations with appreciable ($\neq 0$) fluxes. Around the SLV, they ranged between -7 and $-110 \text{ mmol}\cdot\text{m}^{-2}\cdot\text{d}^{-1}$, whereas on the *Secca dei Pesci*, the oxygen flux was $-82 \text{ mmol}\cdot\text{m}^{-2}\cdot\text{d}^{-1}$.

Table 4. Fluxes of dissolved oxygen measured (as $\text{mmol}\cdot\text{m}^{-2}\cdot\text{d}^{-1}$) by the AdaN benthic chamber around the PVC.

#	Cruise Stations	Flux ($\text{mmol}\cdot\text{m}^{-2}\cdot\text{d}^{-1}$)	R ²
1	PANA13–1	−19.97	0.8192
2	GEOCAL14–1	−7.12	0.8968
3	GEOCAL14–2	−52.92	0.9796
4	PANA14–BP	−110.80	0.9175
5	PANA15A–Piana av	2.93	0.4493
6	PANA15A–PEG1 av	−0.99	0.1474
7	PANA15A–PEG1 min	−34.07	0.9542
8	PANA15A–PEG1 max	−1.70	0.4564
9	PANA15A–SP	−81.73	0.9951
10	PANA15B–1	−15.37	0.9116
11	PANA15B–2	−2.97	0.7456
12	PANA15B 3	−0.77	0.0357
	average	−27.12	
	Standar deviation	36.68	
	Po River prodelta	35.00	

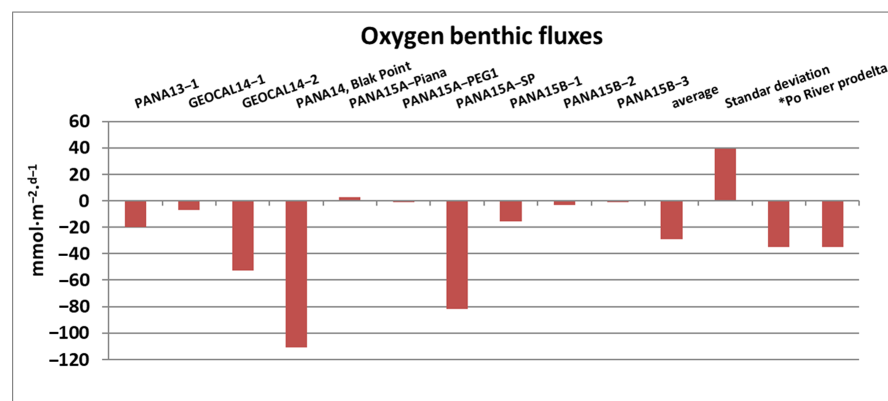


Figure 14. Graphs of dissolved oxygen fluxes measured (as $\text{mmol}\cdot\text{m}^{-2}\cdot\text{d}^{-1}$) by the AdaN around the PVC. Negative values indicate an oxygen decrease in the chamber.

Elements. The elemental analyses were carried out only in the stations around the SLV and at the *Secca dei Pesci* (Table 5, Figure 15). Fe, Mn and, to a lesser extent, Zn and Al showed measurable fluxes at all the stations on the borders of the SLV (PANA13-1, GEOCAL14-1 and GEOCAL14-2) except PANA15B-1, where the fluxes were low (Table 5). On the *Secca dei Pesci* (PANA15A-SP), where the DIC and pH fluxes were the highest, the Fe and Mn fluxes were very low and accompanied by some Ni flux. B was measured only at two stations and showed opposite trends: constant release at PANA13-1 and constant adsorption at GEOCAL14-2.

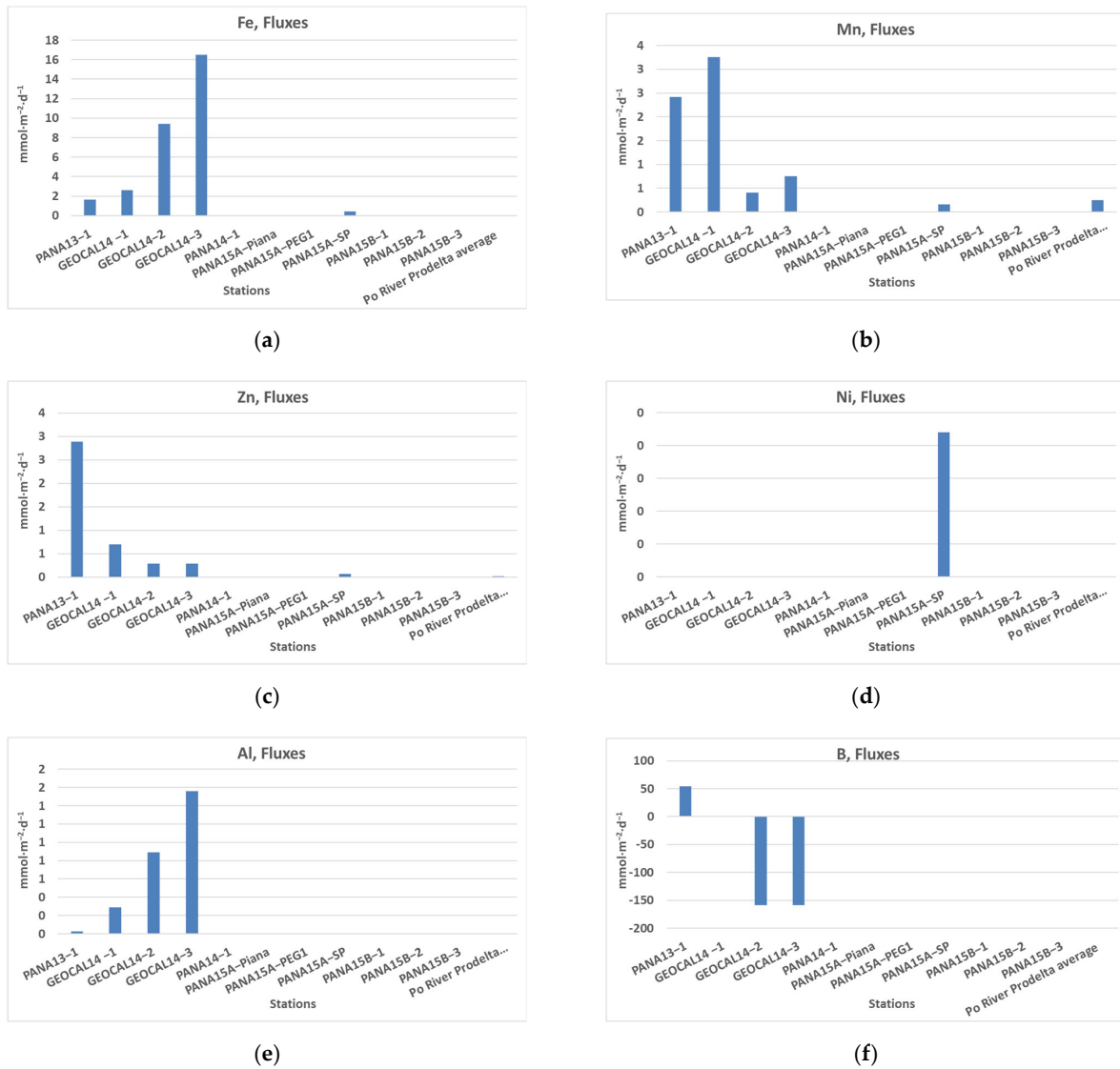


Figure 15. Graphs of the iron (a), manganese (b), zinc (c), nickel (d), aluminum (e), borum (f) fluxes measured (as $\text{mmol}\cdot\text{m}^{-2}\cdot\text{d}^{-1}$) by the AdaN around the PVC.

Table 5. Metal fluxes measured (as $\text{mmol}\cdot\text{m}^{-2}\cdot\text{d}^{-1}$) by the AdaN instruments around the PVC. Red: uncertain flux due to the low R^2 . ND/0 fluxes are assumed to be equal to zero (see text). ND: not determined.

#	Stations	Fe	R ²	Mn	R ²	Zn	R ²	Ni	R ²	Al	R ²	B	R ²
1	PANA13–1	1.66	1	2.41	1	2.88	1	ND	–	0.02	1	54.11	1
2	GEOCAL14–1	2.64	0.84	3.26	1.00	0.70	0.55	ND	–	0.29	0.76	ND	–
3	GEOCAL14–2	9.41		0.41	0.38	0.29	0.89	ND	–	0.89	0.37	–158.99	0.73

Table 5. Cont.

#	Stations	Fe	R ²	Mn	R ²	Zn	R ²	Ni	R ²	Al	R ²	B	R ²
4	PANA14–BP	ND	—	ND	—	ND	—	ND	—	ND	—	ND	—
5	PANA15A–Piana	ND/0	—	ND/0	—	ND/0	—	ND/0	—	ND/0	—	ND/0	—
6	PANA15A–PEG1	ND	—	ND	—	ND	—	ND	—	ND	—	ND	—
7	PANA15A–SP	0.42		0.16	0.48	0.06	0.35	0.02	0.53	ND	—	ND/0	—
8	PANA15B–1	0.01	0.02	−0.0057	0.25	ND	—	ND	—	ND	—	ND	—
9	PANA15B–2	ND/0	—	ND/0	—	ND/0	—	ND/0	—	ND/0	—	ND/0	—
10	PANA15B–3	ND/0	—	ND/0	—	ND/0	—	ND/0	—	ND/0	—	ND/0	—
	Average	2.83		1.56		0.98		0.02		0.40		−52.44	
	Standard deviation	3.82		1.52		1.29				0.44		150.69	
	Po River Prodelta	0.02		0.25		0.012							

3.3. Water Column Data

The water column properties determined by the CTD casts on the depressed area north of the islets (Figure 5a) were thoroughly investigated in May 2014 (GEOCAL14 survey) [43]. The CTD casts in this area showed noticeable environmental peculiarities. The pH profiles highlighted plumes of acidified water (<8) near the sea bottom (Figure 5b) centered on different venting sites (PEG1, PEG8, PANA14-BP and PANA14-2). Several casts showed negative peaks of pH at depths ranging from 44 m to 65 m in the area on the SE border of the SLV. The low pH peaks were associated with a reduction in water transparency, as in the P007 station (Figure 5a for location) at ~60 m and, though less marked, at ~40 m (Figure 16). Furthermore, pH measurements near the bottom by ROV showed much lower values, i.e., 5.8 to 6.5, near the gas venting sites.

DIC. The pCO₂ probe mounted on the ROV allowed us to measure pCO₂ concentrations very close to the emission points. In the areas affected by venting, pCO₂ was very high, ranging between 626.61 and >2009.4 ppm (upper detection limit of the probe) (Table 6, Figure 17).

Table 6. pCO₂ concentrations (in ppm) recorded by the probe mounted on the ROV at the sites affected by the hydrothermal vents (upper detection limit, 2009.4 ppm).

Dives	Maximum pCO ₂ (ppm)	Maximum Depth (m)	Date
Secca dei Pesci (dive 1)	1827.51	65	26 June 2015
Secca dei Pesci (dive 1)	1438.29	65	26 June 2015
Secca dei Pesci (dive 1)	626.61	65	26 June 2015
Secca dei Pesci (dive 2)	2009.40	70	26 June 2015
Smoking Land (dive 3)	2009.40	206	27 June 2015
SW Basiluzzo (dive 4)	2009.40	85	28 June 2015
SW Basiluzzo (dive 5)	1185.98	85	28 June 2015
SW Basiluzzo (dive 6)	1109.71	85	28 June 2015
SW Basiluzzo (dive 7)	831.97	85	28 June 2015
SW Basiluzzo (dive 8)	2009.40	85	29 June 2015
SW Basiluzzo (dive 9)	751.78	70	29 June 2015
SW Basiluzzo (dive 10)	1029.51	70	29 June 2015
Secca del Capo (dive 12)	984.53	230	30 June 2015
Secca del Capo (dive 11)	671.59	70	30 June 2015
Average	1321.08		
Standard deviation	547.30		

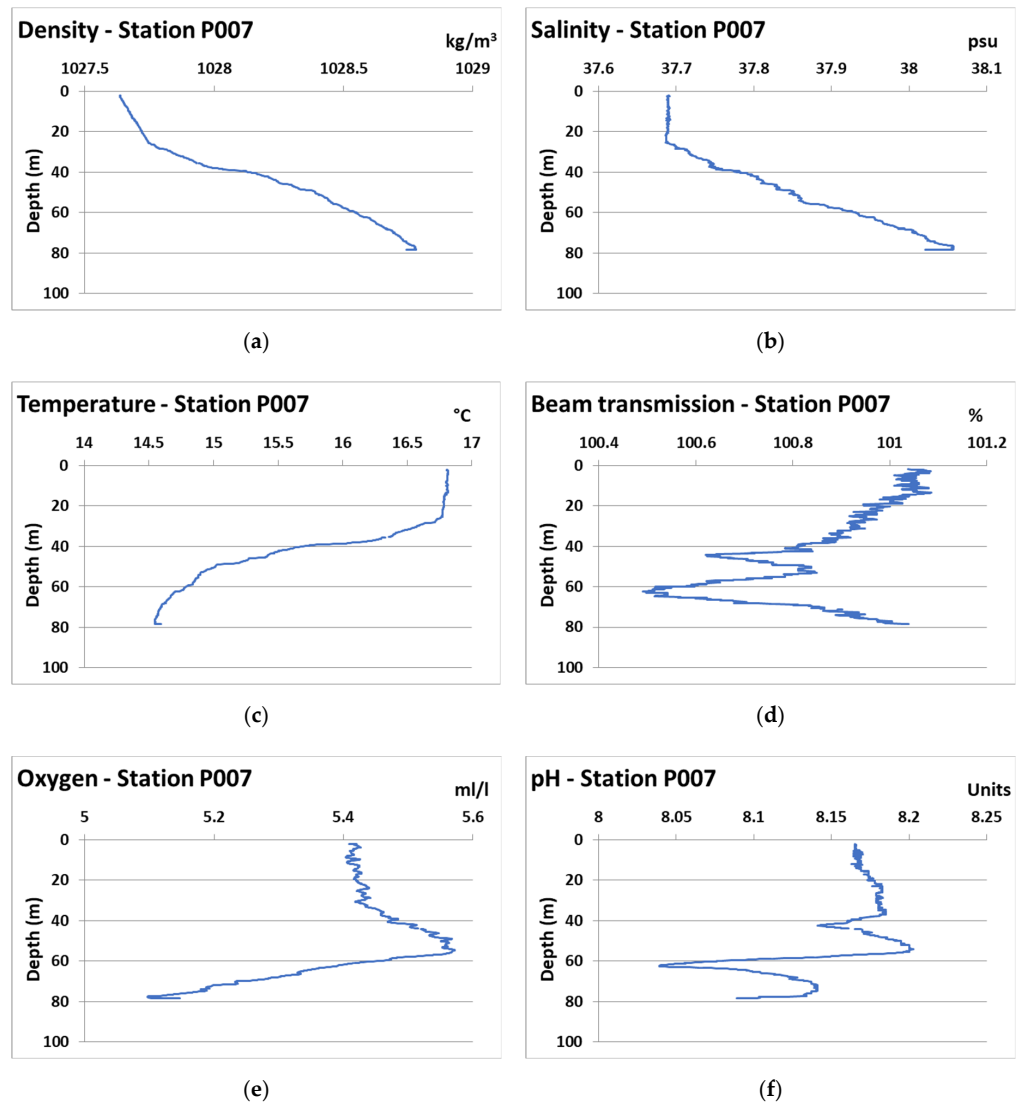


Figure 16. Physicochemical parameters measured during the GEOCAL14 survey at a representative station north of the islets (P007 station, Figure 6 for location), (a) density; (b) salinity; (c) temperature; (d) beam transmission; (e) dissolved oxygen; (f) pH.

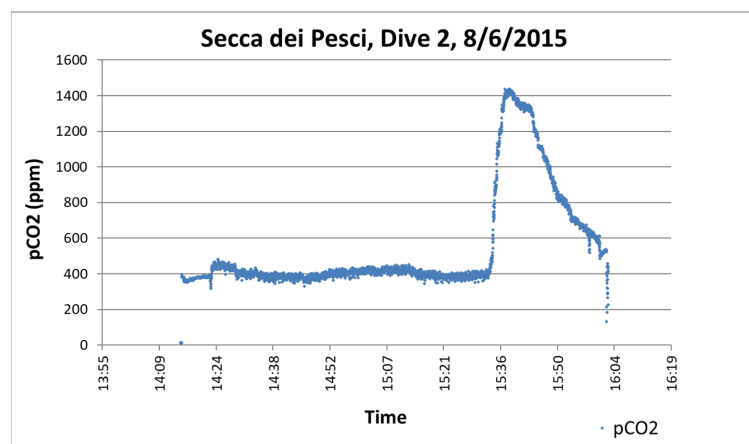


Figure 17. Data recorded by the probe mounted on the ROV during Dive 2 at Secca dei Pesci. The histogram clearly shows the high pCO₂ values close to the emission point; in this case, the maximum value of the pCO₂ is 1438 ppm, which is lower than the upper detection limit of the probe (2009.4 ppm).

At some stations, the seawater present above the sediment in the box-corer and SW104-corer showed a strong effervescence (Figure 18a). The DIC concentrations measured in the water samples collected in these effervescent waters were very high (maximum values 12.23915 mM), whereas in all the other water samples, collected in the water column, the DIC concentrations were in the normal range for seawater.



(a)

(b)

Element	Series	unn. C [wt.%]	norm. C [wt.%]	Atom. C [at.%]	Error (3 Sigma) [wt.%]
Carbon	K-series	4.30	5.23	11.28	2.85
Oxygen	K-series	26.93	32.73	53.01	10.09
Sodium	K-series	4.29	5.21	5.88	0.95
Magnesium	K-series	0.36	0.44	0.47	0.16
Silicon	K-series	2.07	2.51	2.32	0.35
Phosphorus	K-series	0.49	0.60	0.50	0.15
Calcium	K-series	0.16	0.20	0.13	0.10
Iron	K-series	38.16	46.38	21.52	3.15
Sulfur	K-series	0.14	0.17	0.14	0.10
Chlorine	K-series	5.37	6.53	4.77	0.63
Potassium	K-series	0.00	0.00	0.00	0.00
Total:		82.28	100.00	100.00	

(c)

Figure 18. (a) Effervescent seawater over in the box corer sediment just arrived on board; (b) Incoherent sediments covered by a crust of reddish precipitate collected to the SE of the SLV [43]; (c) Geochemical composition of the reddish precipitate of Figure 18b.

Metals. Also, the metal concentrations were higher in the water samples showing effervescence and in the normal range of seawater for the other water column samples.

3.4. Deposit and Crust

The sea bottom around the PVC has been sampled by both the box-corer and SW104 corer [39,43]. The substrate recovered by the box-corer and SW104-corer in the SE of the SLV along the northern slope of the DLBP shoal consisted of incoherent sediments covered by a crust of reddish precipitate (Figure 18b). The seawater lying over the sediment of the

box-corer was strongly effervescing (Figure 18a) and showed a low pH (5.0–6.0). The XRF analysis of the reddish crust allowed us to infer that it consisted of Fe-oxyhydroxides, as deduced by the strong concentrations of iron and oxygen (Figure 18c), the minerals that are also found on the chimney walls [22,28–30].

4. Discussion

Morphological investigations. The detailed geomorphology of the plateau allowed us to highlight narrow, elongated and basically straight slopes as well as throughs and reliefs stretched both from SW to NE and from WSW to ENE; craters and pinnacles were also observed in the same directions (Figures 6–9).

The main slopes, throughs and reliefs are interpreted as tectonic structures, as already delineated in previous works [2,15,16]. The fact that these morphologies outcrop on a sea bottom shaped during the last low stand sea level and the following rising [17] entails the tectonic has been active in the last 10,000–20,000 years. By this way, the active tectonic has affected the sea bottom morphology after the flattening subsequent to the wave erosion during and after the last sea level rise. In particular, the slope on the NW of the Smoking Land Valley and the nodding to the SE are interpreted as an active extensional fault dipping to SE; on the contrary, the weaker slopes on the SE of the Smoking Land Valley and the nodding to the NW are interpreted as active extensional faults dipping to the NW. This tectonic set-up endorses and details the extensional horst-graben and half-graben patterns as the general detachment configuration of the area [12,15,16]. The area is also complicated by several extensional faults, with variable directions, connecting the main SW-NE and WSW-ENE tectonic patterns. A tentative drawing of the normal faults present to the east of Panarea Island is shown in Figure 19.

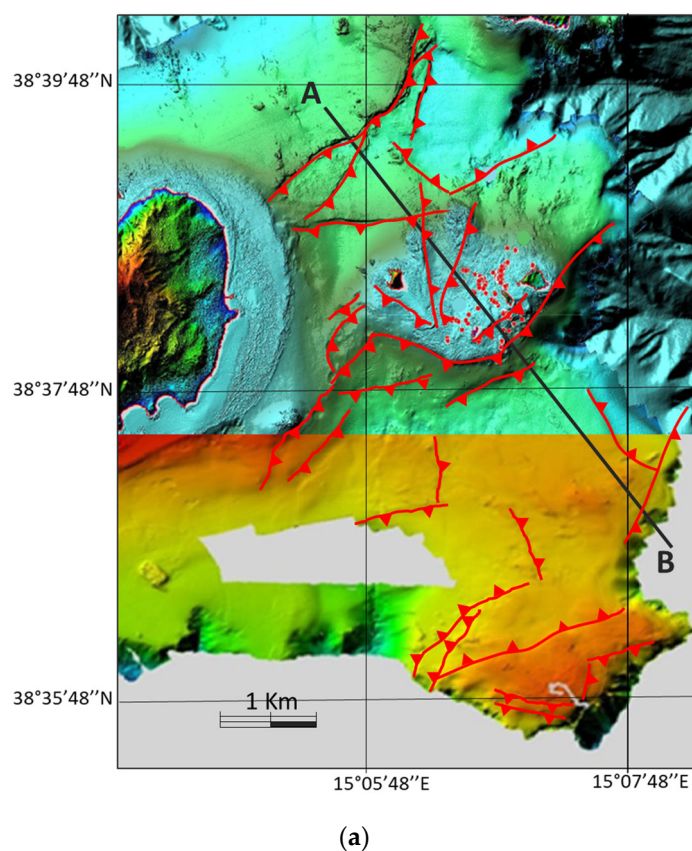


Figure 19. Cont.

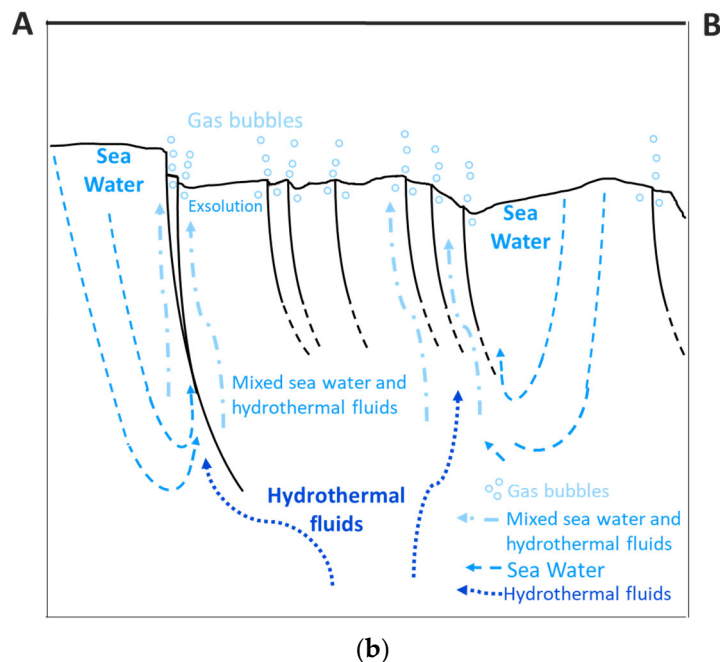


Figure 19. (a) Hypothetical drawing of the tectonic setting based on the detailed seafloor morphology with highlighted normal faults and the horst-grabens structure. In red, the main normal fault is shown. (b) Schematic tectonic structure and fluid and gas circulation beneath the SLV in the A–B section. Black lines: normal faults. Blue drawings: fluid and gas circulation. Dark blue dotted lines: gas rising from the depth; light blue dashed lines: seawater penetrating from the bottom; light blue dotted–dashed lines: mixed seawater and hydrothermal fluids; light blue circles: gas bubbles.

ROV dives. The high-resolution bathymetry also enabled the recognition of active and extinct vent morphology, which was observed in detail by ROV dives, particularly regarding pinnacles and craters. On the northwestern side of the Smoking Land Valley, the pinnacles are grouped in a field of more than 200 units of different sizes, located at the base and stretched in the same direction of the main NE slope [22] (Figure 7). The ROV diving and few pH analyses carried out on board in the water collected near the chimney venting holes [22,28,30,39,43] allowed us to identify these structures as active and extinct vent chimneys (Figure 20). The active chimneys showed both bubbling activity and fluid escaping from the mouths lying on the top or on the lateral sides (Figure 20a,b). The substrate around the active holes are characterized by clear brown walls without any visible sessile benthonic community (Figure 20a,b). The pictures and the video footage from which this was drawn (available on request) show that the gas bubbles are rising, while the fluid is sinking along the chimney walls; this suggests a cold seep age. The extinct chimneys show substrates rich in benthic flora (Figure 20b). The clear brown substrates represent young deposits that have not had time to be colonized, while the flora-rich substrates are older deposits colonized by sessile epibenthic communities.

On the contrary, on the southeastern slope of the Smoking Land Valley, the gas venting morphologies consist of craters of different sizes and a coarse grain-size sea bottom (Figures 4b and 6b–d). Again, in this case, the ROV dives allowed us to establish that these structures are both active, with present gas bubbling (Figure 21), and inactive.

It should be noted that the morphological manifestations of the gas fluid venting are different between the northwestern and the southeastern borders of the Smoking Land Valley, suggesting a different tectonic configuration or fluid composition or geochemical and physical seafloor properties. This difference in the morphological manifestations of the gas fluid venting between the northwestern and the southeastern borders of the Smoking Land Valley could also be due to the depth of the hydrothermal fluid circulation [25]. One or a combination of these reasons result in more continuous seeps on the northwestern border

and in pulsating and bursting seeps on the southeastern border of the SLV producing the different morphologies of the northwestern and southeastern borders.

The ROV dives on the eastern flank of the Ridge NE of Basiluzzo allowed us to ascertain that the scattered chimneys observed on this area are inactive (Figure 20c,d), but, despite this, they are colonized by few observable sessile organisms. This is certainly attributable to the lack of light at this higher depth (more than 140 m) but also to the different composition of the substrate that presents a high sulfur concentration (Figure 20c,d), which could prevent the development of observable organisms [29].

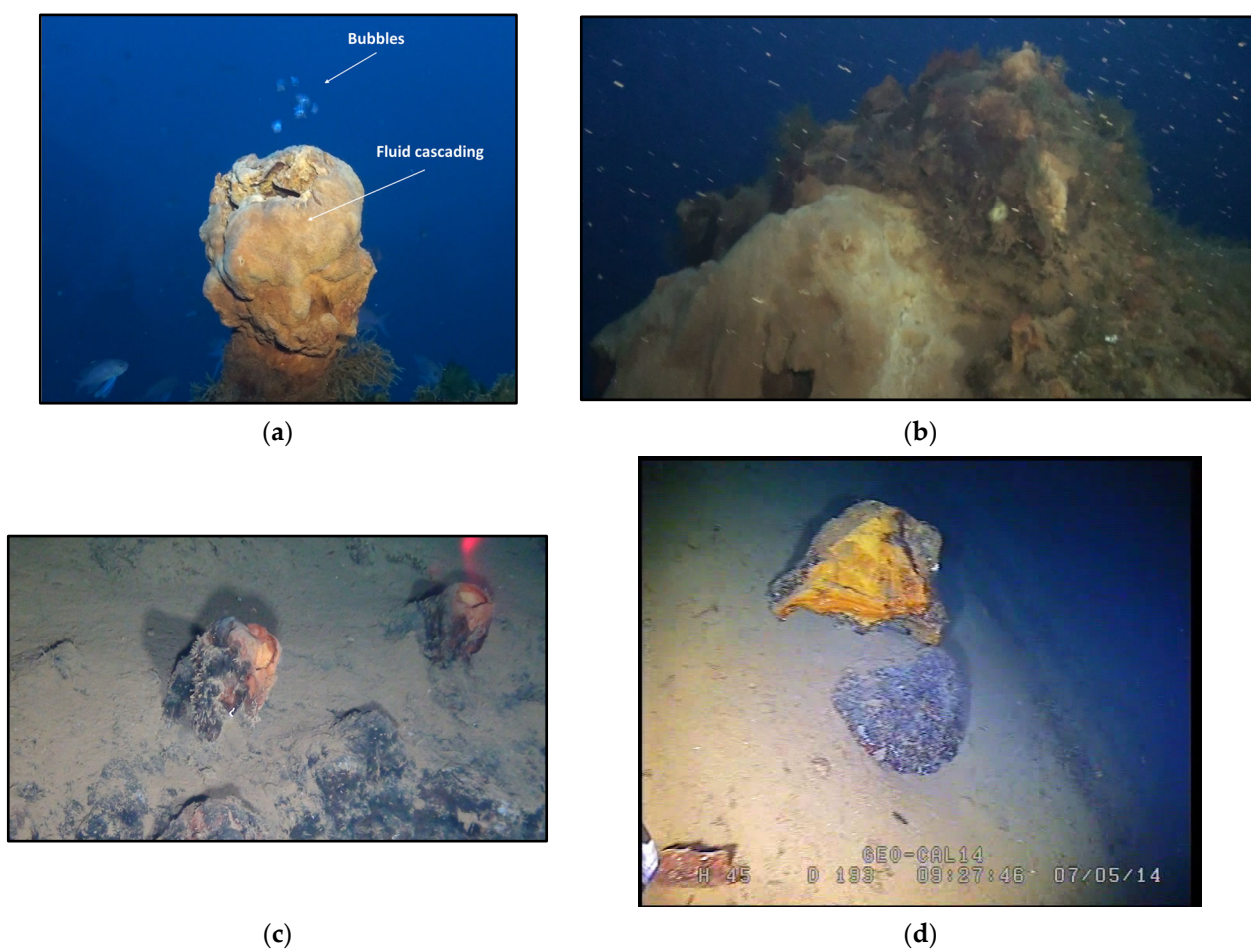


Figure 20. (a) Photograph of an active chimney in the Smoking Land showing bubbles and fluid venting activity and the clear reddish walls without observable flora; (b) extinct chimney in the Smoking Land with walls rich in flora and a lateral, more recent uncolonized deposit; (c) inactive chimneys on the eastern hillside of the ridge to the NE of Basiluzzo Islet with reddish (on the eastern wall) and inside yellow (sulfur) deposits; (d) internal section of an extinct chimney with the external red and dark brown wall and yellow interior sulfur deposit. Pictures from ROV dives.

Regarding the ROV dives in the northern border of the DLBP, the video footage analysis allowed for the identification of a variety of morphological structures of dimensions not detected during the multibeam investigations as well as distinctive benthic communities generated by the release of gases and fluids from the sea bottom (Figure 21). In this area, white bacterial mats thriving around active gas venting on a hard (Figure 21a) and soft (Figure 21b) substrate, scattered mini-cones on a coarse and soft sea bottom (Figure 21c,d), scattered mini-craters on a coarse and mud sea bottom (Figure 21b) and Fe-oxyhydroxide crusts disrupted by active gas venting (Figure 21e) have been detailed.

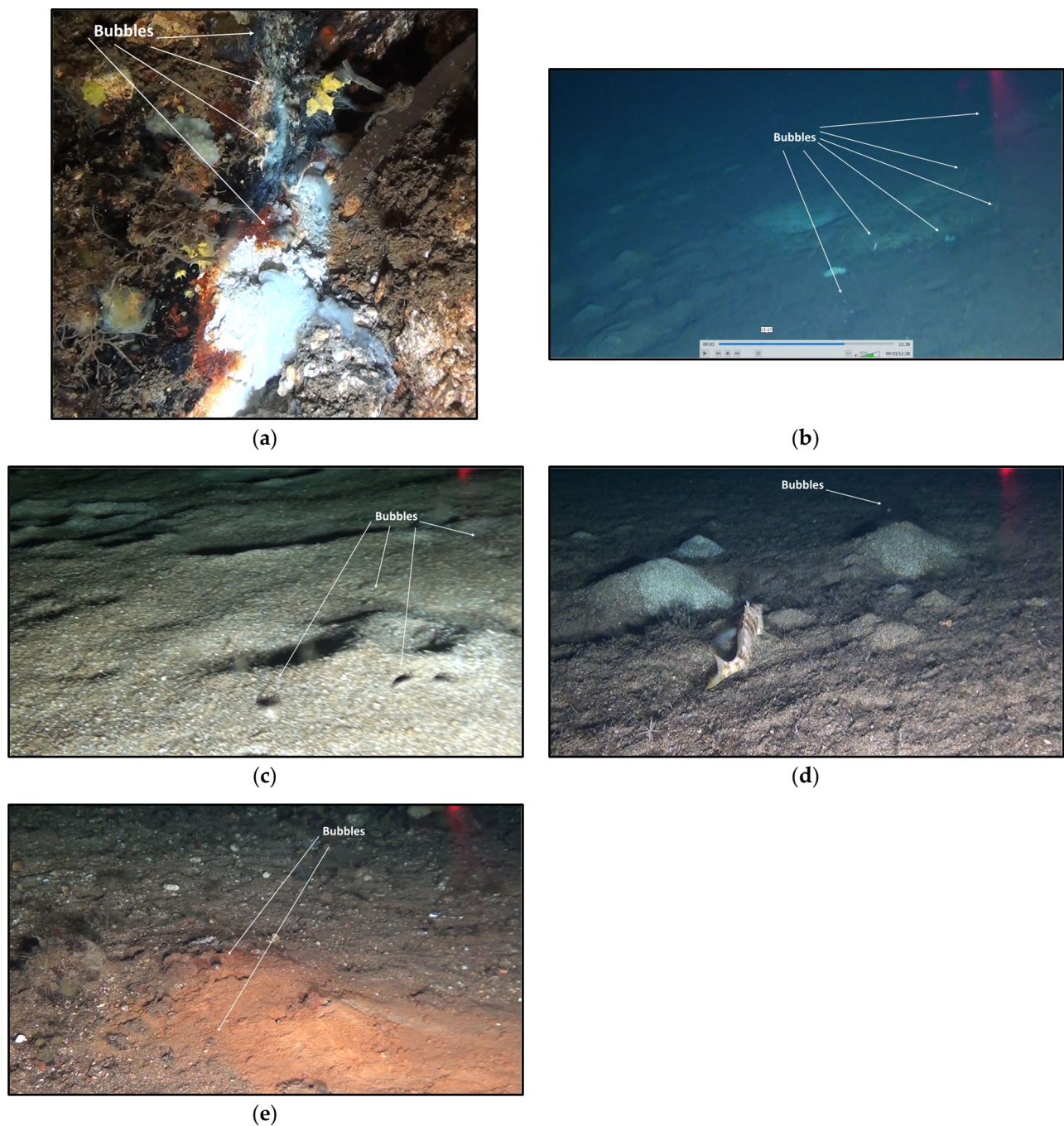


Figure 21. Mini seep morphologies and benthic communities on the southeastern slope of the SLV seafloor; (a) gas venting with bubbles spillage and a bacterial mat (white deposit) around the fissure seep on the hard bottom; (b) scattered mini-crater-like morphologies on the mud seafloor with active gas bubble venting and a white bacterial mat; (c) scattered mini-crater-like structures on a coarse grain-sized seafloor and active gas venting. The picture is taken on the bottom of one crater; it depicts a weak gas-releasing activity as bubbles escaping from the bottom, characterized by a coarse grain size; (d) scattered mini-cone morphologies created by active gas bubble venting; (e) active gas bubble venting on Fe-oxyhydroxide crust.

Dissolved fluxes at the sediment–water interface. Dissolved sediment–water interface flux measurements highlighted strong diffusive seeps in the same area where focused seeps were also described, that is, on the northern border of the Smoking Land Valley, close to the NW slope (GEOCAL14-2), and also on the corrugated relief to the SE of

the Smoking Land Valley (GEOCAL14-1, PANA13-1, PANA15A-PEG1 and PANA14-BP). Diffusive fluxes consisted of acidic and slightly warm solutions rich in DIC and metals (Figures 9–12; Tables 2–5). These two SW-NE extensive areas also contain focused seeps: the Smoking Land chimney field on the NW border and the field comprising several relict craters on the SE margin of the SLV (the Panarea Moon Land, PML). These two areas of high degassing are separated by the Smoking Land Valley depression, which has no measurable diffusive fluxes at the sediment–water interface (PANA15B-2, PANA15A-Piana) (Figures 12–15; Tables 2–5).

These fluxes are exclusively of hydrothermal origin. This was inferred from their strong acidity resulting from strong proton positive fluxes or the pH lowering measured in the benthic chamber, their strong reducing power, inferred by the strong negative Oxygen fluxes, and their very high DIC and metal fluxes, due to direct seepage from the seafloor.

The proton increases or pH reductions into the benthic chamber reflect the release of DIC-rich fluids from the sea bottom. The pH of the fluids released from the sea bottom was <8.2, with probable marked minima below the seafloor where the physical–chemical environment makes predominant carbon species like H_2CO_3 and HCO_3^- . In this setup, when the fluids reach the surface, the pressure suddenly drops and the seawater carbon system unbalances the solution, inducing $\text{CO}_{2(g)}$ exsolution [25,53] and a proton concentration decrease (3).



Then, the solution tends to restore the seawater equilibrium by reverting to (3).

The negative values of dissolved oxygen fluxes on the sea bottom around PVC are due only to the oxidation of the upwelling reduced chemical species. The oxygen consumption must exclusively be attributed to the oxidation of anoxic fluids because of the virtual absence of reactive organic matter on the seafloor. This is supported by the insignificant oxygen consumption and DIC benthic fluxes at sites unaffected by hydrothermal seepage (PANA15A-Piana, PANA15B-2 and PANA15B-3) (Figures 12 and 14), whereas seafloors affected by organic matter mineralization show, in any case, a minimal negative oxygen flux and a positive DIC flux, as in sediments of the Adriatic Sea, where only the flux component due to the mineralization of organic matter is present [54,55] (Tables 2 and 4, Figures 12 and 14). On the other hand, the absence of mineralizable organic matter on the sea bottom of the PVC is usual because of the oligotrophic waters of the Tyrrhenian Sea and the lack of consistent nutrient and organic matter inputs from the mainland.

Moreover, the spatial distribution of both diffusive and focused seepage sources, concentrated on the NW and SE margins of the Smoking Land Valley, combined with the active tectonic structural arrangement of horsts and graben separated by extensional faults (Figure 19) allow for supporting and extending the hydrothermal circulation proposed by [25]. In this case, the gas-rich hydrothermal fluids rise and are released along the outcropping planes of the active extensional faults to the north and through a series of more complex, but still extensional, fractures to the south (Figure 19b). Near the sediment–water interface, the sudden decrease in the hydrostatic pressure also leads to exsolution and the consequent formation of gas bubbles, as detailed in (1). Instead, in the central flat area of the Smoking Land Valley, the absence of fractures in the body of the graben prevents the release of fluids and gases (Figure 19b).

The fact that the fluids released from the bottom are slightly warm and have a salinity similar to that of seawater suggests a quite superficial circulation and an aged process. The fluids seeping on the margins of the graben include the upwelling of deep gas-rich brines, which acidify pore waters. On their way up, the acidic waters leach the volcanic rocks and earlier hydrothermal deposits, dissolving and accumulating metals in the solution. In turn, water rising through the seafloor retrieves the water column seawaters, which then seep underground, creating a circuit (Figure 19b). The seawater percolating from the upper layers of the seafloor mixes with brines rising from the greater depths along the fault planes, creating slightly warmer and less dense solutions, which in turn tend to rise up from the

sea bottom. Then, the gases dissolved in the hydrothermal fluids tend to exsolve when the pressure drops quickly near the sediment–water interface. This is also the explanation for why the fluids seeping from the Smoking Valley chimneys sink in the water column while the gas bubbles rise.

At the stations lying to the SE of the Smoking Land Valley, weak, medium and high diffusive DIC fluxes have been measured (Figure 12, Table 2). In this area, zones with gas-charged sediments underlying thin Fe-oxyhydroxide reddish crusts are found, as inferred by the strongly effervescing water of the box-corer recovered on board (Figures 18 and 21e) [39,43]. In this case, the effervescence is attributed to the fracturing of the reddish crust, leading the exsolution of the dissolved gas. This process suggests that the superficial Fe-hydroxide layer present in this area forms a plug that prevents the release of the underlying gas and pressurized fluids of hydrothermal origin. The Fe-oxyhydroxide crusts here form at the sediment–water interface because metal highly concentrated in the acidic fluids precipitates as metal hydrate oxides ($M_nO_m \cdot H_2O$, $M = \text{Metal}$), mainly amorphous to polymorphous Fe-oxyhydroxides ($\gamma\text{-Fe(O)OH}$), variable from red lepidocrocite to ferrihydrite when they come in contact with the aerobic and less acidic bottom seawaters.

The crater-like structures present at the SE of the Smoking Land Valley are very similar to the more recent structure surveyed at the PEG1 crater site, which detailed the evolution and partial filling after the 2002 burst event [20,38,39]. We think that, in time, PEG1 will probably achieve the same appearance of the scattered relict craters present in this area, and, as a consequence, the several craters similar to the PEG1 site suggest that numerous events like the 2002 burst occurred in the past and created the present Panarea Moon Land. This suggests the hypothesis that explosions like the 2002 event occur frequently and cyclically in the Moon Land and that the seafloor in this area would behave as a pulsating field, where cyclical explosions result in the formation of charged and quiescent areas.

These cyclical explosions could produce serious dangers to people and ecosystems [22,56–58] as a consequence of slides, earthquakes, tsunamis [22,59,60] or modifications of water column properties changing the biota communities or dead zone formation [61–63].

Measurements of the DIC fluxes at the sediment–water interface in the bottom sea around the hydrothermal active area of the PVC were limited in time and concerned only some areas, but they are, in any case, useful in establishing a new hypothesis about the amount of CO_2 released from the seafloor in this area during the Holocene. The last sea level started about 20,000 years ago from the past 100–120 m depth [63]; the horst graben structure to the east of the Panarea depth was submerged during this last sea level rise; therefore, in the past 10,000 years, this area lay in a marine environment with a depth similar to or shallower than that of the present. If we consider that the area is still venting gases and fluids in a steady state status, we can calculate the total CO_2 released in the last 10 kilo-years, as reported by [34].

Regarding the southern margin of the Smoking Land Valley, we can assume the flux measured at the station PANA15B1 ($61.54 \text{ mmol} \cdot \text{m}^{-2} \cdot \text{d}^{-1}$) is representative of the steady state minimum value of this area, since it is not affected by the pulsating events typical of the Panarea Moon Land. The same can be postulated for the slope to the NW of the Smoking Land Valley with respect to the station GEOCAL14-1 ($700 \text{ mmol} \cdot \text{m}^{-2} \cdot \text{d}^{-1}$), which can be considered a steady-state flux value at a ~80 m depth in contrast to the stronger and irregular fluxes of the hydrothermal chimneys of the Smoking Land. Under these assumptions, if we consider a northwestern degassing area of about 0.3 Km^2 , with a mean conservative minimum flux of $1 \text{ mol} \cdot \text{m}^{-2} \cdot \text{d}^{-1}$, and a southeastern degassing area of about 0.5 Km^2 , emitting a mean conservative lower flux of $0.1 \text{ mol} \cdot \text{m}^{-2} \cdot \text{d}^{-1}$, we obtain a total annual flux of carbon of about 1500 t/y emitted by the PVC (4).

$$1 \cdot 12 \cdot 365 \cdot 0.3 + 0.1 \cdot 12 \cdot 365 \cdot 0.5 = 1533 \text{ t/y} \quad (4)$$

Considering a flux integration over the last 10,000 years, from the submersion of the shelf area of the PVC subsequent to the last sea level rise [17], we obtained a value

of ~15 Mt; if we add an additional output of 2.2 Mt of CO₂ due to the burst degassing events [34], we arrive at a total amount of about 17.2 Mt of carbon released from the bottom of the northeastern area of the PVC. This value is comparable to the 19.1 Mt (70 Mt of CO₂) hypothesized by [34], which is based on previous data and a different methodology.

These results are clearly based on data collected only once for each site and only in specific areas that could not be sufficiently representative of the total fluxes, especially if we consider the pulsating features of these hydrothermal processes. For these reasons, this quantification should be taken as a first attempt (as in [34]) of a more accurate quantification and also as a new method that could be added to the regular monitoring of the geochemical and oceanographic processes of the area [64]. Then, this estimation should be improved in the future by new surveys and monitoring activities, allowing for the obtention of more data, both in time and space.

Furthermore, this calculation did not consider the *Secca dei Pesci* area, where the strongest DIC fluxes (~11 mol·m⁻²·d⁻¹) were measured (Figure 12, Table 2), because the data were collected at one station for one time. However, the strong DIC flux at the edge of a SW-NE-stretching horst (Figure 19) suggests that a tectonic extensional pattern, similar to that located NW of Panarea, is also present here, generating hydrothermal circulation and seepage here.

Water column investigations. Regarding the water column, the formation of two negative pH peaks at different depths on the Smoking Land Valley has been detected (Figures 5 and 16). This two-layer low-pH peak setup is supposed to be due to a Ping-Pong-like movement of the venting solutions as a consequence of their density changes with respect to the surrounding waters (Figure 22), as already partially glimpsed by [65] in other volcanic submarine complexes or by [66] in the case of pockmark venting.

In this case, the gas-rich, weak-warmer hydrothermal fluids, released from the seafloor, produce effervescence near the sediment–water interface due to exsolution as a consequence of the sudden pressure decrease, as explained in Process (1) of Figure 22 and Formula (1). This promotes the rise of water masses resulting from the mixing of the acidic and lower-density solutions released from the seafloor with the seawater along the water column (Process 2 of Figure 22). In particular, the venting solutions ascend for the presence of gas bubbles that pull the fluids upward during their rise, and the lower density is due to the higher temperature. As these solutions rise, the gas bubbles are adsorbed and the temperature decreases; thus, the density of the solutions increases and the bubble pulling decreases (Process 3 of Figure 22). When these solutions reach a depth with the same density, which, in this case, coincide with the pycno-cline (Figure 22), they stop their ascension, thus giving rise to the upper low-pH layer (Number 4 of Figure 22). As the gas continues to be absorbed and the temperature decreases, the density still increases, and the solutions sink until they reach a lower layer with the same density (Number 5 of Figure 22), where the solutions stop, giving rise to the second low-pH layer (Number 6 of Figure 22). These migration and mixing processes create the characteristic two-layer low-pH pattern described north of the islets, where gas venting is more frequent and intense (Figures 5, 16 and 22). This reflection process, a Ping-Pong process, would cause the stationing of CO₂-rich seawater under the pycno-cline; then, the CO₂-rich waters would remain trapped in the colder water column for long time until the CO₂ bubbles are completely absorbed, thus preventing CO₂-rich water from reaching the surface and the release of the hydrothermal CO₂ into the atmosphere. This process should then be considered in the CO₂ global budget.

Also, in this case, the data collected in the water column and, in particular, the physical–chemical parameters such as the pH, temperature, salinity and DIC concentrations are spatially and temporally limited so that the proposed explanation for the formation of the two low pH layers should be supported by further investigations and, especially, by synoptic surveys repeated in time, which are, possibly, to be added to the monitoring activities already carried out in the area [65].

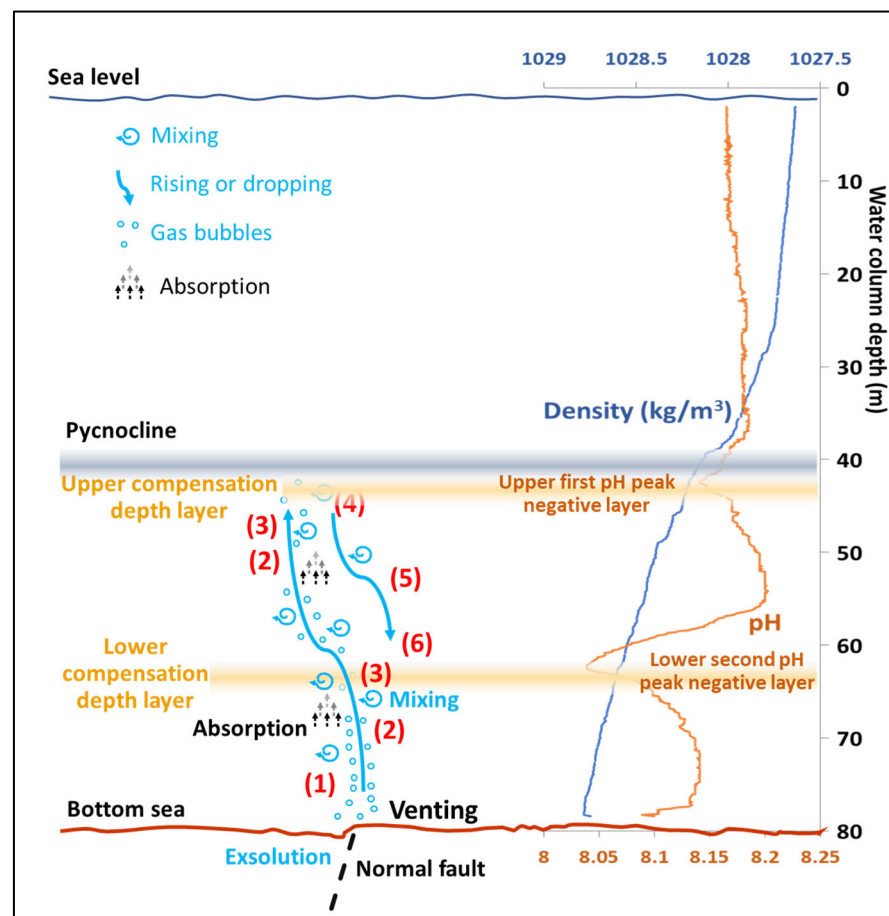


Figure 22. Schematic drawing of the processes leading to the formation of the two pH layers. (1) Gas and fluid venting with bubble formation (exsolution); (2) bubble and fluid rising; (3) gas absorption and increasing density; (4) upper compensation depth layer with the formation of a low pH peak for the stationing of acidic mixed venting and seawater fluids reaching the same density as that of the surrounding seawaters; (5) increasing density and dropping of diluted mixed fluids; (6) the density of the mixed fluids reaches the same density as that of the surrounding seawaters, so they stop the dropping and form the second and lower pH negative peak at the lower compensation depth layer.

The new data about the carbon submarine benthic fluxes of the PVC (1.5 Kt/y) are not comparable to other submarine non-eruptive carbon emissions of other circum-Tyrrhenian volcanic edifices because of the lack of data. Considering the non-eruptive carbon emission of the emergent volcanic edifices of the circum-Tyrrhenian area, between 32 Kt/y (Vulcano) and 570 Kt/y (Stromboli) or 1107 Kt/y (Etna), the carbon submarine benthic fluxes of the PVC are certainly lower but comparable. Furthermore, if the PVC submarine carbon measurements indicate significant carbon emissions in its submerged part, this should most likely also be true for the volcanoes currently active in the Aeolian arc (Stromboli and Vulcano), for the Sicily [67] channel and for the rest of the world [13]. Moreover, the PVC carbon submarine non-eruptive emissions are certainly lower but not negligible compared to the global C submarine volcanic emissions, variable between 595 and 27,545 Kt/y [13]. These last two observations led to highlighting that a real quantification of underwater CO₂ emissions in the Italian seas and, more generally, in marine active volcanic areas should be pursued for an exact calculation of global CO₂ budgets and the capacity of the ocean to adsorb CO₂ and acidify and then the prediction of global climate warming.

5. Conclusions

The morphological, geochemical and visual investigations allowed us to improve the knowledge of the tectonic structure, the venting activity and the biogeochemical processes in the water column around the Panarea Volcanic Complex, as well as the contribution of submarine volcanic areas to the Carbon cycle, carbon budget and acidification process in marine environments and their impact on the atmosphere and global climatic warming.

An SW-NE and WSW-ENE-striking horst-graben and half-graben structure has been detailed between the Panarea and Basiluzzo islands. The structure is characterized by a central depression, the Smoking Land Valley, bounded by extensional faults connected, in turn, by extensional structures. Furthermore, another horst-graben structure was outlined on the *Secca dei Pesci* shoal to the SE of the Panarea Island.

At the edges of the graben, we detailed the occurrence of strong diffusive and focused fluxes of DIC and metal-rich acidic fluid, gas venting and morphologies of active and relict seeps. In this area, the strongest diffusive fluxes have been recorded at the northwestern border of the Smoking Land Valley, at the base of a steep escarpment lined up with minor slopes, and to the south, along a corrugated relief. On the northern boundary, the focused seeps give rise to the formation of a wide number of well-developed hydrothermal chimneys (~200) [22], while on the southeastern border, they lead to the formation crater morphologies: the Panarea Moon Land (PML). Both on the northwestern and the southeastern boundaries, the focused morphologies of chimneys and craters are active and relicts.

These sights better support and outline the hydrothermal circulation proposed by [25]. Hydrothermal fluids rise up along two sub-parallel fault plane systems that bound two reliefs (horsts) separated by a lower plain (the Smoking Land Valley), i.e., the top of a graben; these fault planes favor the vents both as diffusive and focused seeps. As a consequence of this tectonic setting, the diffusive benthic fluxes are not significant in the central plain and strongly variable both in time and in space along the graben edges. Strong diffusive seeps linked to a horst structure have also been measured at the *Secca dei Pesci* shoal. In this last case, the carbon fluxes correspondingly reach their maximum of $11 \text{ mol} \cdot \text{m}^{-2} \cdot \text{d}^{-1}$. These values are very high and should be rapidly measured again and monitored to observe the possible evolution of the system in space and time.

In this context, the acidic fluids, rich in dissolved Iron, induce the formation of oxyhydroxide crusts on the bottom, which form the chimney structures on the northwestern margin and the crater morphologies on the southwestern border of the Smoking Land Valley. On the southeastern margin, these crusts prevent the underlying fluids and gas from seeping up through the seafloor; their buildup over time results in crust breakup and paroxysmal eruptions and then in the formation of crater morphological structures. The process is reminiscent of a pulsating mechanism, where cyclical bursts give rise to charged and discharged areas on the seafloor. This cyclical nature entails that these areas should be continuously monitored for the risk of sudden explosions, as in the 2002 burst event. Moreover, on the northwestern border, the crust buildup leads to the formation of well-developed chimneys that also show cyclic activities, indicated by the relict and active, but not bursting, structures; in any case, it needs to be monitored and protected, as recommended by [22].

On the other hand, if this research highlighted the different morphologies created by the focused seeps, to the north-east (chimneys) and to the south-east (craters), respectively, it has also posed a question: Why these different structures and processes? At the moment, the available data are not able to respond to this question, and it would require dedicated investigations.

The utilization of the benthic chamber allowed us to recognize and measure diffusive venting and to quantify the volcanic DIC released from the seafloor east of Panarea. According to these new experimental data, DIC benthic (1.5 Kt/y) fluxes are comparable to the 19.1 Mt proposed by [34], suggesting that 17.2 Mt of carbon has been released in the past 10,000 years. In any case, our investigations demonstrate that diffusive fluxes, as well

as the focused seeps, are not homogeneously distributed on the sea bottom; rather, they are concentrated along fracture and fault planes and show an irregular and somewhat cyclic time release.

The release of acidic fluids from the sea bottom may alter the chemical–physical structure of the water column, giving rise to two low-pH layers beneath the pycnocline by a Ping-Pong mechanism, which can limit the release of volcanic CO₂ to the atmosphere.

The data herein reported are clearly limited to the sites and times of collection, but, on the other hand, we think that this is the first step for a future improved quantification of the dissolved benthic fluxes in the PVC seafloor. Further sampling and measurements by the benthic chambers and by the collection of additional biogeochemical data from the water column and seafloor would provide valuable insights into the relevant processes.

More generally, the dissolved fluxes at the sediment water interface in a submarine environment would also allow for making a more accurate estimate of the benthic fluxes of DIC and metals of volcanic origin from the bottom and for studying their effects on water column chemical properties, particularly in terms of bottom sea CO₂ emissions affecting ocean acidification, water–air CO₂ exchanges and the ongoing global warming. Important information from dedicated monitoring activities and biogeochemical oceanographical investigations could also enhance the safety and protection of the area, preventing possible accidents due to sudden bursts.

Dedicated oceanographic cruises as well as monitoring activities aimed at measuring the dissolved benthic fluxes and water column biogeochemical properties could be carried out in key places to obtain a sufficient areal variability as well as repeated over time to evaluate the cyclicity of these processes by linking to the already present research and monitoring efforts. Following these considerations, investigating dissolved benthic due to volcanic activity and its effects on biogeochemical seawater properties and processes may provide a new research tool for monitoring the evolution of hydrothermal processes over time and generating scientific data to further the research and discussion about sub-marine volcanic areas.

Author Contributions: Conceptualization, F.S., T.R., S.C. and G.B.; Methodology, F.S., T.R., S.C., V.E., M.G., E.D.B., P.G. and G.B.; Software, F.S., S.C., M.G., E.D.B. and G.B.; Validation, F.S., T.R., F.A., S.C., V.E., M.G., E.D.B., P.G. and G.B.; Formal Analysis, F.S., S.C. and G.B.; Investigation, F.S., T.R., F.A., S.C., V.E., M.G., E.D.B., P.G. and G.B.; Resources, F.S., T.R., F.A., S.C., M.G., E.D.B., P.G. and G.B.; Data Curation, F.S., S.C. and G.B.; Writing—Original Draft Preparation, F.S. and G.B.; Writing—Review and Editing, T.R., S.C. and V.E.; Visualization, F.S.; Supervision, F.S., T.R., S.C. and G.B.; Project Administration, T.R.; Funding Acquisition, F.S., T.R., F.A. and G.B. All authors have read and agreed to the published version of the manuscript.

Funding: The research was funded by D.R.A. Assessorato Territorio Ambiente Regione Siciliana-Asse 3 Linea di intervento 3.2.1.2 of POR FESR Sicilia 2007–2013.

Data Availability Statement: Data are contained within the article.

Acknowledgments: This paper is partly based on an early draft written by the late Giovanni Bortoluzzi some days before his passing. We acknowledge his contribution, but especially his infectious enthusiasm and relentless commitment to research, which have made his scientific career and activity an example for all of us. We are grateful to the crews of the research vessels that participated in the surveys: “*A. Magnaghi*” of Istituto Idrografico Militare, R/V “*Astrea*” of ISPRA, N/O “*Urania*” of CNR and to the colleagues of ISPRA and the SZN, who participated in the field work. We also acknowledge Enrico Bonatti, who supported our work and involved ISMAR since the very beginning. We thank the laboratory of the IMM-CNR of Bologna (Italy) for the XRF analyses. We thank the Coast Guard of Lipari for their logistic support, the friends of Coastal Consulting Exploration of Bari, F. De Giosa and S. Lippolis, the Captain and crew of R/V “*L. Sanzo*” and the Pino Arena of Arenasub. The friendly help and assistance of the inhabitants of Panarea, especially Pina, her husband and her family, made all the difference to all of us. Most maps and figures were generated with the Paul Wessel GMT package. Finally, we would like to remember the work conducted at Panarea and Stromboli in November 2002 and January 2003 by R/V “*Thetis*”, which sunk dramatically in August 2007. The project was partially funded by INGV/Dipartimento Protezione Civile, ISMAR of

CNR and ISPRA. This research was funded by ISPRA grant number PON R&C 2007–2013—Progetto “MARINE HAZARD” (PON03PE_00203). Data regarding the water column and benthic fluxes are free and available on request to federico.spagnoli@cnr.it.

Conflicts of Interest: The authors declare no conflict of interest.

References

1. Billi, A.; Barberi, G.; Faccenna, C.; Neri, G.; Pepe, F.; Sulli, A. Tectonics and seismicity of the Tindari Fault System, southern Italy: Crustal deformations at the transition between ongoing contractional and extensional domains located above the edge of a subducting slab. *Tectonics* **2006**, *25*, TC2006. [[CrossRef](#)]
2. Marani, M.P.; Gamberi, F.; Savelli, C. Shallow-water polymetallic sulfide deposits in the Aeolian island arc. *Geology* **1997**, *25*, 815–818. [[CrossRef](#)]
3. Savelli, C.; Marani, M.; Gamberi, F. Geochemistry of metalliferous, hydrothermal deposits in the Aeolian Arc (Tyrrhenian Sea). *J. Volcanol. Geotherm. Res.* **1999**, *88*, 305–323. [[CrossRef](#)]
4. Gamberi, F.; Savelli, C.; Marani, M.P.; Ligi, M.; Bortoluzzi, G.; Landuzzi, V.; Costa, M. Contesto morfo-tettonico e depositi idrotermali di solfuri ed ossidi di ferro in una porzione sommersa dell’arco eoliano (in base ad indagini ad alta definizione). *Boll. Soc. Geol. Ital.* **1998**, *117*, 55–71.
5. Boatta, F.; D’Alessandro, W.; Gagliano, A.L.; Liotta, M.; Milazzo, M.; Rodolfo-Metalpa, R.; Hall-Spencer, J.M.; Parello, F. Geochemical survey of Levante Bay, Vulcano Island (Italy), a natural laboratory for the study of ocean acidification. *Mar. Pollut. Bull.* **2013**, *73*, 485–494. [[CrossRef](#)] [[PubMed](#)]
6. Barberi, F.; Gandino, A.; Gioncada, A.; La Torre, P.; Sbrana, A.; Zenucchini, C. The deep structure of the Eolian arc (Filicudi-Panarea-Vulcano sector) in light of gravity, magnetic and volcanological data. *J. Volcanol. Geotherm. Res.* **1994**, *61*, 189–206. [[CrossRef](#)]
7. Argnani, A.; Savelli, C. Cenozoic volcanism and tectonics in the Southern Tyrrhenian Sea: Space time distribution and geodynamic significance. *J. Geodyn.* **1999**, *27*, 409–432. [[CrossRef](#)]
8. Argnani, A. The Southern Tyrrhenian Subduction System: Recent Evolution and Neotectonic Implications. *Ann. Geophys.* **2000**, *43*, 585–607. [[CrossRef](#)]
9. Calanchi, N.; Peccerillo, A.; Tranne, C.; Lucchini, F.; Rossi, P.L.; Kempton, P.; Barbieri, W.; Woo, T.W. Petrology and geochemistry of volcanic rocks from the island of Panarea: Implications for mantle evolution beneath the Aeolian island arc (Southern Tyrrhenian sea). *J. Volcanol. Geoth. Res.* **2002**, *115*, 367–395. [[CrossRef](#)]
10. De Astis, G.; Ventura, G.; Vilaro, G. Geodynamic significance of the Aeolian volcanism (Southern Tyrrhenian Sea, Italy) in light of structural, seismological, and geochemical data. *Tectonics* **2003**, *22*, 1040. [[CrossRef](#)]
11. Dekov, V.M.; Savelli, C. Hydrothermal activity in the SE Tyrrhenian Sea: An overview of 30 years of research. *Mar. Geol.* **2004**, *204*, 161–185. [[CrossRef](#)]
12. Lucchi, F.; Tranne, C.A.; Calanchi, N.; Rossi, P. Late Quaternary deformation history of the volcanic edifice of Panarea, Aeolian Arc. *Bull. Volcanol.* **2007**, *69*, 239–257. [[CrossRef](#)]
13. Frezzotti, M.L.; Peccerillo, A.; Panza, G. Earth’s CO₂ degassing in Italy. *J. Virtual Explor.* **2010**, *36*, 21. [[CrossRef](#)]
14. Argnani, A.; Serpelloni, E.; Bonazzi, C. Pattern of deformation around the central Aeolian Island: Evidence from multichannel seismics and GPS data. *Terra Nova* **2007**, *19*, 317–323. [[CrossRef](#)]
15. Gabbianelli, G.; Gillot, P.Y.; Lanzafame, G.; Romagnoli, C.; Rossi, P.L. Tectonic and volcanic evolution of Panarea (Aeolian islands, Italy). *Mar. Geol.* **1990**, *92*, 313–326. [[CrossRef](#)]
16. Gamberi, F.; Marani, M.; Savelli, C. Tectonic, volcanic and hydrothermal features of a submarine portion of the Aeolian arc (Tyrrhenian Sea). *Mar. Geol.* **1997**, *140*, 167–181. [[CrossRef](#)]
17. Romagnoli, C. Characteristics and morphological evolution of the Aeolian volcanoes from the study of submarine portions. Geological Society, London. *Memoirs* **2013**, *37*, 13–26. [[CrossRef](#)]
18. Esposito, A.; Giordano, G.; Anzidei, M. The 2002–2003 submarine gas eruption at Panarea volcano Aeolian Islands, Italy: Volcanology of the seafloor and implications for the hazard scenario. *Mar. Geol.* **2006**, *227*, 119–134. [[CrossRef](#)]
19. Italiano, F.; Nuccio, P.M. Geochemical investigations of submarine exhalations to the east of Panarea, Aeolian Islands, Italy. *J. Volcanol. Geoth. Res.* **1991**, *46*, 125–141. [[CrossRef](#)]
20. Aliani, L.S.; Bortoluzzi, G.; Caramanna, G.; Raffa, F. Seawater dynamics and environmental settings after November 2002 gas eruption off Bottaro (Panarea, Aeolian Islands, Mediterranean Sea). *Cont. Shelf Res.* **2010**, *30*, 1338–1348. [[CrossRef](#)]
21. Anzidei, M.; Esposito, A.; Bortoluzzi, G.; Degiosa, F. The high resolution map of the exhalative area of Panarea (Aeolian Is., Italy). *Ann. Geophys.* **2005**, *48*, 899–921.
22. Esposito, V.; Andaloro, F.; Canese, S.; Bortoluzzi, G.; Bo, M.; Di Bella, M.; Italiano, F.; Sabatino, G.; Battaglia, P.; Consoli, P.; et al. Exceptional discovery of a shallow-water hydrothermal site in the SW area of Basiluzzo islet (Aeolian archipelago, South Tyrrhenian Sea): An environment to preserve. *PLoS ONE* **2018**, *13*, e0190710. [[CrossRef](#)] [[PubMed](#)]
23. Dekov, V.; Kamenov, G.; Abrasheva, M.; Capaccioni, B.; Munnik, F. Mineralogical and geochemical investigation of seafloor massive sulfides from Panarea Platform (Aeolian Arc, Tyrrhenian Sea). *Chem. Geol.* **2013**, *335*, 136–148. [[CrossRef](#)]

24. Peters, M.; Strauss, H.; Petersen, S.; Kummer, N.-A.; Thomazo, C. Hydrothermalism in the Tyrrhenian Sea: Inorganic and microbial sulfur cycling as revealed by geochemical and multiple Sulphur isotope data. *Chem. Geol.* **2011**, *280*, 217–231. [[CrossRef](#)]
25. Price, R.E.; La Rowe, D.E.; Italiano, F.; Savov, I.; Pichler, T.; Amend, J.P. Subsurface hydrothermal processes and the bioenergetics of chemolithoautotrophy at the shallow-sea vents off Panarea Island (Italy). *Chem. Geol.* **2015**, *407*, 21–45. [[CrossRef](#)]
26. Bortoluzzi, G.; Aliani, A.; D’Orlando, F.; Ligi, M.; Riminucci, F.; Carmisciano, C.; Cocchi, L.; Muccini, F. Multidisciplinary investigations at Panarea (Aeolian Islands) after the exhalative crisis of 2002. In *Marine Research at CNR*; Brugnoli, E., Cavarretta, G., Mazzola, S., Trincardi, F., Ravaioli, M., Santoleri, R., Eds.; CNR: Rome, Italy, 2010; Volume DTA/06-2011, ISSN 2239-5172.
27. Tudino, T.; Bortoluzzi, G.; Aliani, S. Shallow-water gaseohydrothermal plume studies after massive eruption at Panarea, Aeolian Islands, Italy. *J. Mar. Syst.* **2014**, *131*, 1–9. [[CrossRef](#)]
28. Bortoluzzi, G.; Spagnoli, F.; Aliani, S.; Romeo, T.; Canese, S.; Esposito, V.; Grassi, M.; Masetti, G.; D’Alti, L.; Cocchi, L.; et al. New geological, geophysical and biological insights on the hydrothermal system of the Panarea—Basiluzzo Volcanic complex (Aeolian Islands, Tyrrhenian Sea). *Rend. Online Della Soc. Geol. Ital.* **2014**, *31*, 403.
29. Bortoluzzi, G.; Romeo, T.; La Cono, V.; La Spada, G.; Smedile, F.; Esposito, V.; Sabatino, G.; Di Bella, M.; Canese, S.; Scotti, G.; et al. Ferrous iron-and ammonium-rich diffuse vents support habitat-specific communities in a shallow hydrothermal field off the Basiluzzo Islet (Aeolian Volcanic Archipelago). *Geobiology* **2017**, *15*, 664–677. [[CrossRef](#)]
30. Spagnoli, F.; Andaloro, F.; Canese, S.; Capaccioni, B.; Esposito, V.; Giordano, P.; Romeo, T.; Bortoluzzi, G. Nuove recenti conoscenze sul sistema idrotermale del complesso vulcanico dell’Isola di Panarea (Arcipelago delle Eolie, Mar Tirreno Meridionale). New recent insights of the hydrothermal system of the Panarea Island (Aeolian Archipelago, South Tyrrhenian Sea). *Mem. Descr. Carta Geol. d’It.* **2019**, *105*, 85–90.
31. Capaccioni, B.; Tassi, F.; Vaselli, D.; Tedesco, D.; Rossi, P.L. The November 2002 degassing event at Panarea Island (Italy): The results of a 5 months geochemical monitoring program. *Ann. Geophys.* **2005**, *48*, 755–765.
32. Capaccioni, B.; Tassi, F.; Vaselli, O.; Tedesco, D.; Poreda, R. Submarine gas burst at Panarea Island (Southern Italy) on 3 November 2002: A magmatic versus hydrothermal episode. *J. Geophys. Res.* **2007**, *112*, B05201. [[CrossRef](#)]
33. Chiodini, G.; Caliro, S.; Caramanna, G.; Granieri, D.; Minopoli, C.; Moretti, R.; Perrotta, L.; Ventura, G. Geochemistry of the submarine gaseous emissions of Panarea (Aeolian Islands, Southern Italy): Magmatic vs. hydrothermal origin and implications for volcanic surveillance. *Pure Appl. Geophys.* **2006**, *163*, 759–780. [[CrossRef](#)]
34. Monecke, T.; Petersen, S.; Hannington, M.D.; Anzidei, M.; Esposito, A.; Giordano, G.; Garbe-Shonberg, N.A.D.; Melchert, B.; Hocking, M. Explosion craters associated with shallow submarine gas venting off Panarea Island, Italy. *Bull. Volcanol.* **2012**, *74*, 1937–1944. [[CrossRef](#)]
35. Gugliandolo, C.; Italiano, F.; Maugeri, T. The submarine hydrothermal system of Panarea (Southern Italy): Biogeochemical processes at the thermal fluids—Sea bottom interface. *Ann. Geophys.* **2006**, *49*, 783–792. [[CrossRef](#)]
36. Tassi, F.; Capaccioni, B.; Caramanna, G.; Cinti, D.; Montegrossi, G.; Pizzino, L.; Quattrocchi, F.; Valselli, O. Low-pH waters discharging from submarine vents at Panarea Island (Aeolian Islands, southern Italy) after the 2002 gas blast: Origin of hydrothermal fluids and implications for volcanic surveillance. *Appl. Geochem.* **2009**, *24*, 246–254. [[CrossRef](#)]
37. Manini, E.; Luna, G.M.; Corinaldesi, C.; Zeppilli, D.; Bortoluzzi, G.; Caramanna, G.; Raffa, F.; Danovaro, R. Prokaryote diversity and virus abundance in shallow hydrothermal vents of the Mediterranean Sea (Panarea Island) and the Pacific Ocean (North Sulawesi-Indonesia). *Microb. Ecol.* **2008**, *55*, 626–639. [[CrossRef](#)] [[PubMed](#)]
38. D’Alti, L.; De Lucia, A.; Marziani, F.; Niccolini, A.; Zeppetella, A.; di Fava, M.; Guideri, M.; Carmisciano, C.; Cocchi, L.; Muccini, F.; et al. Rapporto sulle attività geofisiche, oceanografiche e di campionamento durante la crociera Panstr12 con Nave Aretusa: Isole Eolie (Stromboli, Panarea, Salina) (2012-06-30–2012-07-14). *Rapp. Tec. INGV* **2013**, *245*, 26.
39. Grassi, M.; D’Alti, L.; Masetti, G.; Filippone, M.; Ricci, E.; Pratellesi, M.; Bortoluzzi, G.; Spagnoli, F.; Borgognoni, L.; Aliani, S.; et al. *Rapporto Sulle Attività Oceanografiche, Geochimiche, Geologiche, Geofisiche e di Campionamento Durante la Crociera PAN13 con Nave Magnaghi: Panarea, I. Eolie, Tirreno, S. Orientale, 2013-06-02–2013-06-08*; Istituto Idrografico della Marina Militare: Genova, Italy, 2013; p. 26.
40. Bortoluzzi, G.; Carrara, G.; Fabretti, P.; Gamberi, F.; Marani, M.; Penitenti, D.; Stanghellini, G.; Tonani, M.; Zitellini, N.; Bonazzi, C.; et al. *Swath Bathymetry and Geophysical Survey of the Tyrrhenian Sea*; Report on Bathymetric, Magnetic and Gravimetric Investigations during Cruises TIR96 and TIR99; IGM-CNR: Bologna, Italy, 1999.
41. Marani, M.P.; Gamberi, F.; Bortoluzzi, G.; Carrara, G.; Ligi, M.; Penitenti, D. Tyrrhenian sea bathymetry. In *From Seafloor to Deep Mantle: Architecture of the Tyrrhenian Backarc Basin*; Marani, M.P., Gamberi, F., Bonatti, E., Eds.; Memoir Carta Geologica D’Italia: Rome, Italy, 2004.
42. Bortoluzzi, G.; Ligi, M.; Cuffaro, M.; D’Orlando, F.; Ferrante, V.; Partescano, E.; Redini, F.; Remia, A.; Riminucci, F.; Romagnoli, C.; et al. *Rapporto Preliminare Sulle Indagini di Sismica a Riflessione e Rifrazione, Morfobatimetriche e Magnetometriche nel Complesso Dell’isola di PANAREA (Eolie, Tirreno Meridionale)*; Crociera Pana 07 Con La N/O Urania (01/09-Agosto-2007); ISMAR: Bologna, Italy, 2007.
43. Loreto, M.F.; Bortoluzzi, G.; Dalpasso, E.; Ferrante, V.; Giordano, P.; Ligi, M.; Spagnoli, F.; Cocchi, L.; Muccini, F.; Canese, S.; et al. *GEO-CAL 2014. Geofisica, Geochimica e Geologia al Largo Della Calabria Occidentale*; Rapporto Tecnico 2014, 129; ISMAR-CNR: Bologna, Italy, 2014.
44. Fabris, M.; Baldi, P.; Anzidei, M.; Pesci, A.; Bortoluzzi, G.; Aliani, S. High resolution topographic model of Panarea Island by fusion of photogrammetric, lidar and bathymetric digital terrain models. *Photogramm. Rec.* **2010**, *25*, 382–401. [[CrossRef](#)]

45. Heinicke, J.; Italiano, F.; Maugeri, R.; Merkel, B.; Pohl, T.; Schipek, M.; Braun, T. Evidence of tectonic control on active arc volcanism: The Panarea-Stromboli tectonic link inferred by submarine hydrothermal vents monitoring (Aeolian arc, Italy). *Geophys. Res. Lett.* **2009**, *36*, L04301. [[CrossRef](#)]
46. Acocella, V.; Neri, M.; Walter, T.R. Structural features of Panarea volcano in the frame of the Aeolian Arc (Italy): Implications for the 2002–2003 unrest. *J. Eodyn.* **2009**, *47*, 288–292. [[CrossRef](#)]
47. Walter, T.R.; Wang, R.; Acocella, V.; Neri, M.; Grosser, H.; Zschau, J. Simultaneous magma and gas eruptions at three volcanoes in southern Italy: An earthquake trigger? *Geology* **2009**, *37*, 251–254. [[CrossRef](#)]
48. Caliro, S.; Caracausi, A.; Chiodini, G.; Ditta, M.; Italiano, F.; Longo, M.; Minopoli, C.; Nuccio, P.M.; Paonita, A.; Rizzo, A. Evidence of a recent input of magmatic gases into the quiescent volcanic edifice of Panarea, Aeolian Islands, Italy. *Geophys. Res. Lett.* **2004**, *31*, L07619. [[CrossRef](#)]
49. Caracausi, A.; Ditta, M.; Italiano, F.; Longo, M.; Nuccio, P.M.; Paonita, A.; Rizzo, A. Changes in fluid geochemistry and physico-chemical conditions of geothermal systems caused by magmatic input: The recent abrupt outgassing off the island of Panarea (Aeolian Islands, Italy). *Geochim. Cosmochim. Acta* **2005**, *69*, 3045–3059. [[CrossRef](#)]
50. Spagnoli, F.; Penna, P.; Giuliani, G.; Masini, L.; Martinotti, V. The AMERIGO Lander and the Automatic Benthic Chamber (CBA): Two New Instruments to Measure Benthic Fluxes of Dissolved Chemical Species. *Sensors* **2019**, *19*, 2632. [[CrossRef](#)] [[PubMed](#)]
51. Spagnoli, F.; Giuliani, G.; Martinotti, V.; Masini, L.; Penna, P. AMERIGO and CBA: A new lander and a new automatic benthic chamber for dissolved benthic flux measurements. In Proceedings of the 2018 IEEE International Workshop on Metrology for the Sea (MetroSea 2018), Bari, Italy, 8–10 October 2018; pp. 206–211. [[CrossRef](#)]
52. Spagnoli, F. Device for Extracting Total Dissolved Inorganic Carbon from an Aqueous Solution and Analysis System Comprising This Device. Patent n. 102016000048914, 3 December 2018.
53. Konno, U.; Tsunogai, U.; Nakagawa, F.; Nakaseama, M.; Ishibashi, J.I.; Nunoura, T.; Nakamura, K.I. Liquid CO₂ venting on the seafloor: Yonaguni Knoll IV hydrothermal system, Okinawa Trough. *Geophys. Res. Lett.* **2006**, *33*, L16607. [[CrossRef](#)]
54. Frascari, F.; Spagnoli, F.; Marcaccio, M.; Giordano, P. Anomalous Po river flood event effects on sediments and water column of the Northwestern Adriatic Sea. *Clim. Res.* **2006**, *31*, 151–165. [[CrossRef](#)]
55. Spagnoli, F.; Dell’Anno, A.; De Marco, A.; Dinelli, E.; Fabiano, M.; Gadaleta, M.V.; Ianni, C.; Loiacono, F.; Manini, E.; Marini, M.; et al. Biogeochemistry, grain size and mineralogy of the central and southern Adriatic Sea sediments: A review. *Chem. Ecol.* **2010**, *26*, 19–44. [[CrossRef](#)]
56. Gilchrist, J.T.; Jellinek, A.M.; Hooft, E.E.E.; Wanket, S. Submarine terraced deposits linked to periodic collapse of caldera-forming eruption columns. *Nat. Geosci.* **2023**, *16*, 446–453. [[CrossRef](#)]
57. Yuen, D.A.; Scruggs, M.A.; Spera, F.J.; Zheng, Y.; Hu, H.; McNutt, S.R.; Thompson, G.; Mandli, K.; Keller, B.R.; Wei, S.S.; et al. Under the surface: Pressure-induced planetary-scale waves, volcanic lightning, and gaseous clouds caused by the submarine eruption of Hunga Tonga-Hunga Ha’apai volcano. *Earthq. Res. Adv.* **2022**, *2*, 100134. [[CrossRef](#)]
58. Zorn, E.U.; Orynbaikyzy, A.; Plank, S.; Babeyko, A.; Darmawan, H.; Robbany, I.F.; Walter, T.R. Identification and ranking of subaerial volcanic tsunami hazard sources in Southeast Asia. *Nat. Hazards Earth Syst. Sci.* **2022**, *22*, 3083–3104.
59. Lynett, P.; McCann, M.; Zhou, Z.; Renteria, W.; Borrero, J.; Greer, D.; Fa’anunu, O.; Bosserelle, C.; Jaffe, B.; La Selle, S.P.; et al. Diverse tsunamigenesis triggered by the Hunga Tonga-Hunga Ha’apai eruption. *Nature* **2022**, *609*, 728–733. [[CrossRef](#)] [[PubMed](#)]
60. Ariza, A.; Kaartvedt, S.; Røstad, A.; Garijo, J.C.; Arístegui, J.; Fraile-Nuez, E.; Hernández-León, S. The Submarine Volcano Eruption off El Hierro Island: Effects on the Scattering Migrant Biota and the Evolution of the Pelagic Communities. *PLoS ONE* **2014**, *9*, e102354. [[CrossRef](#)] [[PubMed](#)]
61. Sotomayor-García, A.; Rueda, J.L.; Sánchez-Guillamón, O.; Urrea, J.; Vázquez, J.T.; Palomino, D.; Fernández-Salas, L.M.; López-González, N.; González-Porto, M.; Santana-Casiano, J.M.; et al. First macro-colonizers and survivors around tagoro submarine Volcano, Canary Islands, Spain. *Geosciences* **2019**, *9*, 52. [[CrossRef](#)]
62. Caramanna, G.; Sievert, S.M.; Bühring, S.I. Submarine Shallow-Water Fluid Emissions and Their Geomicrobiological Imprint: A Global Overview. *Front. Mar. Sci.* **2021**, *8*, 727199. [[CrossRef](#)]
63. Siddall, M.; Rohling, E.J.; Almogi-Labin, A.; Hemleben, C.; Meischner, D.; Schmelzer, I.; Smeed, D.A. Sea-level fluctuations during the last glacial cycle. *Nature* **2003**, *423*, 853–858. [[CrossRef](#)] [[PubMed](#)]
64. Romano, D.; Gattuso, A.; Longo, M.; Caruso, C.; Lazzaro, G.; Corbo, A.; Italiano, F. Hazard scenarios related to submarine volcanic-hydrothermal activity and advanced monitoring strategies: A study case from the Panarea volcanic group (aeolian islands, Italy). *Geofluids* **2019**, *2019*, 8728720. [[CrossRef](#)]
65. Santana-Casiano, J.M.; Fraile-Nuez, E.; González-Dávila, M.; Baker, E.T.; Resing, J.A.; Walker, S.L. Significant discharge of CO₂ from hydrothermalism associated with the submarine volcano of El Hierro Island. *Sci. Rep.* **2016**, *6*, 25686. [[CrossRef](#)]
66. Nardelli, B.B.; Budillon, F.; Watteaux, R.; Ciccone, F.; Conforti, A.; De Falco, G.; Di Martino, G.; Innagi, S.; Tonielli, R.; Iudicone, D. Pockmark morphology and turbulent buoyant plumes at a submarine spring. *Cont. Shelf Res.* **2017**, *148*, 19–36. [[CrossRef](#)]
67. Coltelli, M.; Cavallaro, D.; D’Anna, G.; D’Alessandro, A.; Grassa, F.; Mangano, G.; Patanè, D.; Gresta, S. Exploring the submarine graham bank in the Sicily Channel. *Ann. Geophys.* **2016**, *59*, S0208. [[CrossRef](#)]

Disclaimer/Publisher’s Note: The statements, opinions and data contained in all publications are solely those of the individual author(s) and contributor(s) and not of MDPI and/or the editor(s). MDPI and/or the editor(s) disclaim responsibility for any injury to people or property resulting from any ideas, methods, instructions or products referred to in the content.